Monte Carlo treatment of hadronic interactions in enhanced Pomeron scheme: I. QGSJET-II model

S. Ostapchenko[*]

NTNU, Institutt for fysikk, 7491 Trondheim, Norway

D.V. Skobeltsyn Institute of Nuclear Physics, Moscow State University, 119992 Moscow, Russia

January 18, 2011

Abstract

The construction of a Monte Carlo generator for high energy hadronic and nuclear collisions is discussed in detail. Interactions are treated in the framework of the Reggeon Field Theory, taking into consideration enhanced Pomeron diagrams which are resummed to all orders in the triple-Pomeron coupling. Soft and "semihard" contributions to the underlying parton dynamics are accounted for within the "semihard Pomeron" approach. The structure of cut enhanced diagrams is analyzed; they are regrouped into a number of subclasses characterized by positively-defined contributions which define partial weights for various "macro-configurations" of hadronic final states. An iterative procedure for a Monte Carlo generation of the structure of final states is described. The model results for hadronic cross sections and for particle production are compared to experimental data.

1   Introduction

Nowadays Monte Carlo (MC) generators of hadronic interactions are standard tools for data analysis in high energy collider and cosmic ray (CR) fields. The idea behind employing such MC models is twofold. First of all, they provide a bridge between rigorous theoretical approaches and corresponding experimental studies, thus allowing to confront novel ideas against observations. On the other hand, MC simulations are an inevitable part of contemporary experimental analysis procedures, a measurement of new phenomena depending crucially on the understanding of the corresponding detector response and of the contribution of the "standard" hadronic physics which is mimicked with the help of the MC tools.

In particular, hadronic interaction models play an important role in investigations of very high energy cosmic rays. Because of the extremely low flux of such ultra-energetic particles, they can not be detected directly. Instead one infers their properties from measured characteristics of nuclear-electro-magnetic cascades, so-called extensive air showers (EAS), induced by them in the atmosphere. The corresponding analysis relies crucially on the MC treatment of the cascade development, most importantly, of its backbone - the cascade of hadron-nucleus (nucleus-nucleus) interactions in the atmosphere. The peculiarity of cosmic ray applications of hadronic interaction generators is related to the fact that one has to treat hadronic collisions at energies orders of magnitude higher than ones of present day colliders and that EAS characteristics depend strongly on model predictions for very forward spectra of secondary particles. As a consequence, CR interaction models, like DPMJET [1], EPOS [2], QGSJET [3], or SYBILL [4], which are designed

---

[*]e-mail: sergey.ostapchenko@ntnu.no

to treat general inelastic hadronic collisions, are developed in the framework of the Reggeon Field Theory (RFT) [5], which allows one to take into consideration contributions from both "soft" and "hard" parton dynamics to the interaction mechanism.

Soft nonperturbative interactions are described as soft Pomeron exchanges and dominate hadronic collisions at large impact parameters, thus giving important contributions to total, inelastic, and diffractive hadron-nucleus (nucleus-nucleus) cross sections. On the other hand, at sufficiently high energies the role of so-called semihard hadronic collisions which involve partons of moderately large virtualities is significantly enhanced, the smallness of the corresponding strong coupling being compensated by large collinear and infra-red logarithms and by high density of small x partons. A convenient way to include such processes in the RFT treatment is provided by the "semihard Pomeron" approach [6, 7] where the perturbative part of an "elementary" semihard rescattering is described within the DGLAP formalism, which is preceded by nonperturbative parton cascades ("soft preevolution") described as soft Pomeron emissions.

Additionally, high parton densities reached in "central" collisions of hadrons and, especially, nuclei result in significant nonlinear corrections to the interaction dynamics, related to parton shadowing and saturation [8]. In MC generators, such effects are typically accounted for in a phenomenological way, via energy-dependent parametrizations of some model parameters. The drawback of such constructions is evident: with nonlinear effects dominating the interaction mechanism in the very high energy limit, model predictions are governed by the choice of the corresponding empirical parametrization, rather than by the underlying theoretical approach.

In this work, we choose an alternative way, treating nonlinear interaction effects in the RFT framework as Pomeron-Pomeron interactions [9, 10, 11], based on the recent progress in the resummation of the corresponding, so-called enhanced, RFT diagrams [12, 13, 14]. A MC implementation of such an approach has been hampered for a long time by two factors. First, with the energy increasing, enhanced graphs of more and more complicated topologies start to contribute significantly to the scattering amplitude and to partial cross sections for particular hadronic final states. Thus, dealing with enhanced diagrams, all-order resummation of the corresponding contributions is a must, both for elastic scattering diagrams and for the cut diagrams representing particular inelastic processes. Secondly, it is quite nontrivial to split the complete set of cut enhanced diagrams into separate classes characterized by positively-defined contributions which could be interpreted probabilistically and employed in a MC simulation procedure. While the first problem has been addressed in [12, 13, 14], the MC implementation of the approach is discussed in the present work. Here we mainly address the construction of the model while the results for various particle production processes and applications of the model for calculations of EAS development will be the subject of the forthcoming publication [15].

The outline of the paper is as follows. In Section 2, the calculation of hadron-hadron scattering amplitude is discussed, taking into account enhanced diagram contributions. In Section 3, we consider unitarity cuts of elastic scattering diagrams and define partial contributions for various "macro-configurations" of the interaction, which are employed in the corresponding MC procedure, as described in Section 4. Finally, in Section 5, we discuss characteristic features of the developed model, calibration of model parameters, and present the model results for various hadronic cross sections.

2   Hadron-hadron scattering amplitude

In the RFT approach, high energy hadron-hadron scattering amplitude is defined by multiple scattering graphs of the kind depicted in Fig. 1. The elementary rescattering contributions correspond to independent parton cascades developing between the projectile and target hadrons, which are described by Pomeron exchanges, and to parton cascades which strongly overlap in the phase space and interact with each other, which is described as Pomeron-Pomeron interactions. Thus, applying the multichannel (Good-Walker-like) eikonal scheme [16, 17] to account for contributions of
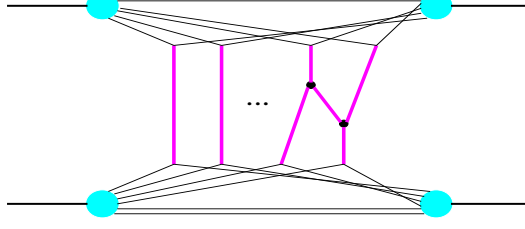
Figure **1**: General multi-Pomeron contribution to hadron-hadron scattering amplitude; elementary scattering processes correspond to Pomeron exchanges (vertical thick lines) or to Pomeron-Pomeron interactions.

small mass intermediate states between Pomeron emissions, elastic hadron a - hadron d scattering amplitude is defined as [13]

$$f_{ad}(s,b) = i \sum_{j,k} C_{j/a} C_{k/d} \left[1 - e^{-\frac{1}{2}\Omega_{ad(jk)}(s,b)} \right] \tag{1}$$

$$\Omega_{ad(jk)}(s,b) = 2\chi^{\mathbb{P}}_{ad(jk)}(s,b) + 2\chi^{\mathrm{enh}}_{ad(jk)}(s,b). \tag{2}$$

Here s and b are c.m. energy squared and impact parameter for the interaction, $C_{j/a}$ defines partial weight for hadron a elastic scattering eigenstate $|j\rangle$ ($|a\rangle = \sum_j \sqrt{C_{j/a}}|j\rangle$, $\sum_j C_{j/a} = 1$), $\chi^{\mathbb{P}}_{ad(jk)}$ and $\chi^{\mathrm{enh}}_{ad(jk)}$ are eikonals corresponding to an exchange of a Pomeron or of an irreducible enhanced (Pomeron-Pomeron interaction) graph between the projectile and target hadrons, the latter being represented by eigenstates $|j\rangle$ and $|k\rangle$.

In this work, we use the "semihard Pomeron" approach [6, 7] to account for contributions of both nonperturbative soft processes and of "semihard" ones, the latter corresponding to parton cascades which develop at least partly in the perturbative region of relatively high virtualities $|q^2| > Q_0^2$, Q_0^2 being some cutoff for pQCD being applicable. Describing the former as phenomenological soft Pomerons and the latter by "semihard Pomeron" exchanges, the "general Pomeron" eikonal is given by the sum of the two contributions:

$$\chi^{\mathbb{P}}_{ad(jk)}(s,b) = \chi^{\mathbb{P}_{\mathrm{soft}}}_{ad(jk)}(s,b) + \chi^{\mathbb{P}_{\mathrm{sh}}}_{ad(jk)}(s,b). \tag{3}$$

The soft Pomeron eikonal $\chi^{\mathbb{P}_{\mathrm{soft}}}_{ad(jk)}$ is expressed via Pomeron emission vertices $N^{\mathbb{P}}$ and the Pomeron propagator $D^{\mathbb{P}}$ as

$$\chi^{\mathbb{P}_{\mathrm{soft}}}_{ad(jk)}(s,b) = \frac{1}{8\pi^2\,i\,s} \int d^2q\, e^{-i\,\vec{q}\vec{b}} \int dx_1\,dx_2\, N^{\mathbb{P}}_{j/a}(x_1,q^2)\, N^{\mathbb{P}}_{k/d}(x_2,q^2)\, D^{\mathbb{P}}(x_1 x_2 s, q^2), \tag{4}$$

where

$$D^{\mathbb{P}}(\hat{s},t) = 8\pi\,i\,s_0\,(\hat{s}/s_0)^{\alpha_{\mathbb{P}}}\, e^{\alpha'_{\mathbb{P}}\,\ln(s/s_0)\,t}, \tag{5}$$

with $\alpha_{\mathbb{P}}$ and $\alpha'_{\mathbb{P}}$ being the intercept and the slope of the Pomeron Regge trajectory and $s_0 \simeq 1\ \mathrm{GeV}^2$ - the hadronic mass scale.

The Pomeron emission vertices are parametrized as

$$N^{\mathbb{P}}_{j/a}(x,t) = \gamma_{j/a}\, e^{\Lambda_{j/a}\,t}\, x^{-\alpha_{\mathrm{part}}}\, (1-x)^{\alpha_{\mathrm{lead}}}, \tag{6}$$

where the exponents $\alpha_{\mathrm{part}} \simeq 0$ and α_{lead} are related to intercepts of secondary Regge trajectories [18, 7].

The semihard contribution $\chi^{\mathbb{P}_{\mathrm{sh}}}_{ad(jk)}$ corresponds to a piece of QCD parton ladder sandwiched between two soft Pomerons (see Fig. 2) and is defined as [7, 19]
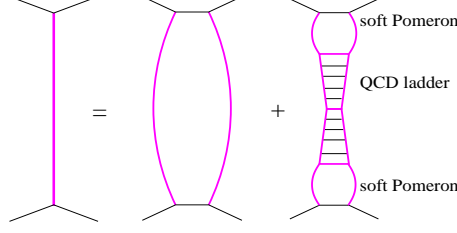
3

Figure **2**: A "general Pomeron" (l.h.s.) consists of the soft and semihard ones - correspondingly the 1st and the 2nd contributions in the r.h.s.

$$\chi_{ad(jk)}^{\mathbb{P}_{\mathrm{sh}}}(s,b) = \frac{1}{32\pi^2 s_0^2} \int d^2q \, e^{-i\vec{q}\vec{b}} \int dx_1 \, dx_2 \, N_{j/a}^{\mathbb{P}}(x_1,q^2) \, N_{k/d}^{\mathbb{P}}(x_2,q^2) \int dx^+ \, dx^-$$

$$\times \, \mathfrak{Im}D^{\mathbb{P}}(s_0/x^+,q^2) \, \mathfrak{Im}D^{\mathbb{P}}(s_0/x^-,q^2) \sum_{I,J=g,q_s} g_I(x^+) \, g_J(x^-) \, \sigma_{IJ}^{\mathrm{QCD}}(x^+x^-x_1x_2s,Q_0^2), \qquad (7)$$

where the vertices g_I for parton I (gluon or sea quark)[1] coupling to the soft Pomeron are parametrized as

$$g_g(z) = r_g \, (1 - w_{qg}) \, (1-z)^{\beta_g}$$

$$g_{q_s}(z) = r_g \, w_{qg} \int_z^1 dy \, y^{\alpha_{\mathbb{P}}-1} \, P_{qg}(y) \, (1-z/y)^{\beta_g}, \qquad (8)$$

with $P_{qg}(y)$ being the Altarelli-Parisi splitting function and the constant r_g being fixed by momentum conservation for parton distribution functions (PDFs).

The contribution $\sigma_{IJ}^{\mathrm{QCD}}(x^+x^-s,Q_0^2)$ of parton ladder with the virtuality cutoff Q_0^2 and with the leg-parton types I, J and light cone momentum fractions x^+, x^- is defined in a standard way (see, e.g. [7, 19])

$$\sigma_{IJ}^{\mathrm{QCD}}(\hat{s},Q_0^2) = K \sum_{I',J'} \int dz^+ \, dz^- \int dp_t^2 \, E_{I\to I'}^{\mathrm{QCD}}(z^+,Q_0^2,M_{\mathrm{F}}^2) \, E_{J\to J'}^{\mathrm{QCD}}(z^-,Q_0^2,M_{\mathrm{F}}^2)$$

$$\times \frac{d\sigma_{I'J'}^{2\to2}(z^+z^-\hat{s},p_t^2)}{dp_t^2} \, \Theta(M_{\mathrm{F}}^2 - Q_0^2), \qquad (9)$$

with $d\sigma_{IJ}^{2\to2}/dp_t^2$ being the differential parton-parton cross section, p_t - parton transverse momentum in the hard process, M_{F}^2 - the factorization scale (here $M_{\mathrm{F}}^2 = p_t^2/4$), and with $E_{I\to I'}^{\mathrm{QCD}}(z,Q_0^2,Q^2)$ describing the evolution of the parton density from the virtuality scale Q_0^2 to Q^2. The factor $K \simeq 1.5$ is designed to take effectively into account higher order QCD corrections.

The idea behind Eq. (7) is to split parton evolution in an elementary scattering process in two parts: i) nonperturbative soft one described phenomenologically by the soft Pomeron asymptotics; ii) parton cascading at $|q^2| > Q_0^2$, treated within the DGLAP formalism. The former is characterized by a significant parton diffusion in the transverse plane and, in the absence of nonlinear corrections, forms parton (sea quark or gluon) momentum and impact parameter distributions at the virtuality scale Q_0^2 [7, 19, 20]. During the latter, parton transverse displacements can be neglected, leaving only the momentum-dependent part, Eq. (9), which is characterized by a stronger energy-rise compared to the soft Pomeron amplitude and drives therefore the high energy behavior of the semihard contribution (7).

To calculate enhanced diagram contributions, we adopt multi-Pomeron vertices of the form [11]

$$G^{(m,n)} = G \, \gamma_{\mathbb{P}}^{m+n}, \qquad (10)$$

---

[1]For brevity, we do not discuss explicitly valence quark contributions to the semihard eikonal; the corresponding description can be found elsewhere [7, 19].
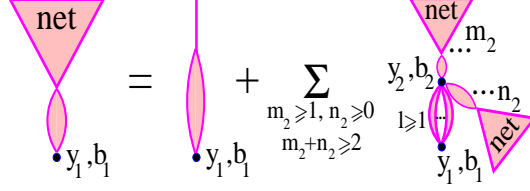
Figure **3**: Recursive equation for projectile net-fan contribution $\chi^{\text{net}}_{a(j)|d(k)}(y_1, \vec{b}_1 | Y, \vec{b})$; y_1 and b_1 are rapidity and impact parameter distances between the projectile proton and the vertex in the handle of the fan. The vertex $(y_2, \vec{b}_2)$ couples together m_2 projectile net-fans and n_2 target net-fans. In addition, there are $l \geq 1$ irreducible 2-point sequences of Pomerons and Pomeron loops, exchanged between the vertices $(y_1, \vec{b}_1)$ and $(y_2, \vec{b}_2)$.

where m and n are numbers of Pomerons connected to the vertex from the projectile, respectively target, side $(m + n \geq 3)$ and the constant G is related to the triple-Pomeron coupling $r_{3\mathbb{P}}$ as $G = r_{3\mathbb{P}}/(4\pi\gamma_{\mathbb{P}}^3)$.

The eikonal $\chi^{\mathbb{P}}_{a(j)}(y, b)$ for a "general Pomeron" exchange between hadron a (represented by eigenstate $|j\rangle$) and a multi-Pomeron vertex, the two being separated from each other by rapidity y and transverse distance b, also receives contributions from both soft and semihard processes

$$\chi^{\mathbb{P}}_{a(j)}(y, b) = \chi^{\mathbb{P}_{\text{soft}}}_{a(j)}(y, b) + \chi^{\mathbb{P}_{\text{sh}}}_{a(j)}(y, b), \tag{11}$$

with the partial contributions $\chi^{\mathbb{P}_{\text{soft}}}_{a(j)}$ and $\chi^{\mathbb{P}_{\text{sh}}}_{a(j)}$ being defined similarly to (4), (7) [20]:

$$\chi^{\mathbb{P}_{\text{soft}}}_{a(j)}(y, b) = \frac{\gamma_{\mathbb{P}}}{8\pi^2 \, i \, s_0 \, e^y} \int d^2q \, e^{-i\,\vec{q}\,\vec{b}} \int dx_1 \, N^{\mathbb{P}}_{j/a}(x_1, q^2) \, D^{\mathbb{P}}(x_1 s_0 \, e^y, q^2) \tag{12}$$

$$\chi^{\mathbb{P}_{\text{sh}}}_{a(j)}(y, b) = \frac{\gamma_{\mathbb{P}}}{32\pi^2 s_0^2} \int d^2q \, e^{-i\,\vec{q}\,\vec{b}} \int dx_1 \, N^{\mathbb{P}}_{j/a}(x_1, q^2) \int dx^+ \, dx^- \, \mathfrak{Im}D^{\mathbb{P}}(s_0/x^+, q^2)$$
$$\times \, \mathfrak{Im}D^{\mathbb{P}}(s_0/x^-, q^2) \sum_{I,J=g,q_s} g_I(x^+) \, g_J(x^-) \, \sigma^{\text{QCD}}_{IJ}(x^+ x^- x_1 s_0 \, e^y, Q_0^2), \tag{13}$$

where we included the vertex factors $\gamma_{\mathbb{P}}$ into the definition of the eikonals.

Similarly, for a Pomeron exchange between two multi-Pomeron vertices separated by rapidity and impact parameter distances y and b we use

$$\chi^{\mathbb{P}}(y, b) = \chi^{\mathbb{P}_{\text{soft}}}(y, b) + \chi^{\mathbb{P}_{\text{sh}}}(y, b) \tag{14}$$

$$\chi^{\mathbb{P}_{\text{soft}}}(y, b) = \frac{\gamma_{\mathbb{P}}^2}{8\pi^2 \, i \, s_0 \, e^y} \int d^2q \, e^{-i\,\vec{q}\,\vec{b}} \, D^{\mathbb{P}}(s_0 \, e^y, q^2) \tag{15}$$

$$\chi^{\mathbb{P}_{\text{sh}}}(y, b) = \frac{\gamma_{\mathbb{P}}^2}{32\pi^2 s_0^2} \int d^2q \, e^{-i\,\vec{q}\,\vec{b}} \int dx^+ \, dx^- \, \mathfrak{Im}D^{\mathbb{P}}(s_0/x^+, q^2) \, \mathfrak{Im}D^{\mathbb{P}}(s_0/x^-, q^2)$$
$$\times \sum_{I,J=g,q_s} g_I(x^+) \, g_J(x^-) \, \sigma^{\text{QCD}}_{IJ}(x^+ x^- s_0 \, e^y, Q_0^2). \tag{16}$$

The above-defined eikonals can be used to calculate the total contribution of irreducible enhanced Pomeron graphs $\chi^{\text{enh}}_{ad(jk)}$. As demonstrated in [12, 13], the latter can be expressed via contributions of subgraphs of certain structure, so-called "net-fans". Those are defined by the Schwinger-Dyson equation of Fig. 3 and correspond to arbitrary irreducible "nets" of Pomerons, with neighboring net "cells" being connected to each other by 2-point sequences of Pomerons and Pomeron loops and with one vertex in the net having a fixed position in the rapidity and impact
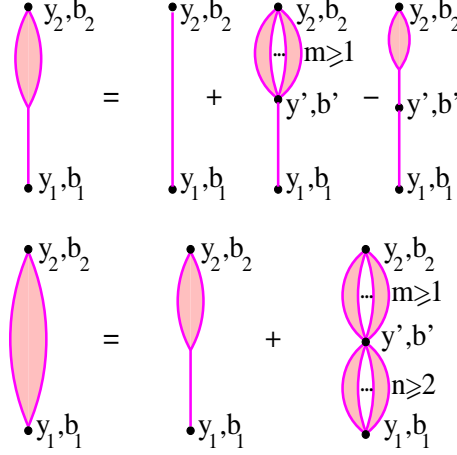
5

Figure 4: Recursive representations for the contributions of irreducible 2-point sequences of Pomerons and Pomeron loops $\chi^{\text{loop}(1)}$ (top) and χ^{loop} (bottom), exchanged between the vertices $(y_1, \vec{b}_1)$ and $(y_2, \vec{b}_2)$.

parameter space.[2] The corresponding equation

$$\chi^{\text{net}}_{a(j)|d(k)}(y_1, \vec{b}_1 | Y, \vec{b}) = \chi^{\text{loop}}_{a(j)}(y_1, b_1) + G \int_\xi^{y_1 - \xi} dy_2 \int d^2 b_2 \left(1 - e^{-\chi^{\text{loop}}(y_1 - y_2, |\vec{b}_1 - \vec{b}_2|)}\right)$$

$$\times \left[\left(1 - e^{-\chi^{\text{net}}_{a(j)|d(k)}(y_2, \vec{b}_2 | Y, \vec{b})}\right) e^{-\chi^{\text{net}}_{d(k)|a(j)}(Y - y_2, \vec{b} - \vec{b}_2 | Y, \vec{b})} - \chi^{\text{net}}_{a(j)|d(k)}(y_2, \vec{b}_2 | Y, \vec{b})\right] \quad (17)$$

involves the contribution $\chi^{\text{loop}}(y_1 - y_2, |\vec{b}_1 - \vec{b}_2|)$ of irreducible 2-point sequences of Pomerons and Pomeron loops, exchanged between the vertices $(y_1, \vec{b}_1)$ and $(y_2, \vec{b}_2)$ (2nd graph in the r.h.s. of Fig. 3), and the contribution $\chi^{\text{loop}}_{a(j)}(y_1, b_1)$ of Pomeron loop sequences exchanged between the vertex $(y_1, \vec{b}_1)$ and hadron a, with a single Pomeron coupled to hadron a (1st graph in the r.h.s. of the Figure). The y_2 integration in the 2nd term in the r.h.s. of (17) is performed between ξ and $y_1 - \xi$, with ξ being the minimal rapidity interval for the Pomeron asymptotics to be applicable. As discussed in [20], net-fan eikonals $\chi^{\text{net}}_{a(j)|d(k)}$ are related to parton (sea quark and gluon) distributions which are probed during hadron-hadron interaction and are thus influenced by rescattering processes on the partner hadron.

As in [14], we define the contribution $\chi^{\text{loop}}(y_1 - y_2, |\vec{b}_1 - \vec{b}_2|)$ and a part of it $\chi^{\text{loop}(1)}(y_1 - y_2, |\vec{b}_1 - \vec{b}_2|)$, corresponding to Pomeron loop sequences which start from a single Pomeron coupled to the vertex $(y_1, \vec{b}_1)$, via Schwinger-Dyson equations of Fig. 4, which gives

$$\chi^{\text{loop}(1)}(y_2 - y_1, |\vec{b}_2 - \vec{b}_1|) = \chi^{\mathbb{P}}(y_2 - y_1, |\vec{b}_2 - \vec{b}_1|) + G \int_{y_1 + \xi}^{y_2 - \xi} dy' \int d^2 b' \, \chi^{\mathbb{P}}(y' - y_1, |\vec{b}' - \vec{b}_1|)$$

$$\times \left[1 - e^{-\chi^{\text{loop}}(y_2 - y', |\vec{b}_2 - \vec{b}'|)} - \chi^{\text{loop}(1)}(y_2 - y', |\vec{b}_2 - \vec{b}'|)\right] \quad (18)$$

$$\chi^{\text{loop}}(y_2 - y_1, |\vec{b}_2 - \vec{b}_1|) = \chi^{\text{loop}(1)}(y_2 - y_1, |\vec{b}_2 - \vec{b}_1|) + G \int_{y_1 + \xi}^{y_2 - \xi} dy' \int d^2 b'$$

$$\times \left[1 - e^{-\chi^{\text{loop}}(y' - y_1, |\vec{b}' - \vec{b}_1|)} - \chi^{\text{loop}}(y' - y_1, |\vec{b}' - \vec{b}_1|)\right] \left[1 - e^{-\chi^{\text{loop}}(y_2 - y', |\vec{b}_2 - \vec{b}'|)}\right]. \quad (19)$$

In turn, for the contribution $\chi^{\text{loop}}_{a(j)}(y_1, b_1)$ and a part of it $\chi^{\text{loop}(1)}_{a(j)}(y_1, b_1)$, corresponding to

___

[2]The 2-point sequence of Pomerons and Pomeron loops, coupled to this vertex, will be referred to as the "handle of the fan".

irreducible Pomeron loop sequences with a single Pomeron coupled to the vertex $(y_1, \vec{b}_1)$, this leads to recursive equations [14]

$$\chi_{a(j)}^{\text{loop}}(y_1, b_1) = \chi_{a(j)}^{\mathbb{P}}(y_1, b_1) + G \int_{\xi}^{y_1 - \xi} dy' \int d^2 b' \; \chi_{a(j)}^{\mathbb{P}}(y', b')$$

$$\times \left[1 - e^{-\chi^{\text{loop}}(y_1 - y', |\vec{b}_1 - \vec{b}'|)} - \chi^{\text{loop}(1)}(y_1 - y', |\vec{b}_1 - \vec{b}'|) \right] \qquad (20)$$

$$\chi_{a(j)}^{\text{loop}(1)}(y_1, b_1) = \chi_{a(j)}^{\mathbb{P}}(y_1, b_1) + G \int_{\xi}^{y_1 - \xi} dy' \int d^2 b' \; \left[\chi_{a(j)}^{\text{loop}}(y', b') - \chi_{a(j)}^{\text{loop}(1)}(y', b') \right]$$

$$\times \chi^{\mathbb{P}}(y_1 - y', |\vec{b}_1 - \vec{b}'|). \qquad (21)$$

Finally, for the total contribution of irreducible enhanced graphs $\chi_{ad(jk)}^{\text{enh}}$ (exchanged between eigenstates $|j\rangle$ and $|k\rangle$ of the projectile and of the target respectively) to elastic scattering amplitude one obtains [13, 14]

$$\chi_{ad(jk)}^{\text{enh}}(s, b) = G \int_{\xi}^{Y - \xi} dy_1 \int d^2 b_1 \; \left\{ \left[\left(1 - e^{-\chi_{a(j)|d(k)}^{\text{net}}} \right) \left(1 - e^{-\chi_{d(k)|a(j)}^{\text{net}}} \right) - \chi_{a(j)|d(k)}^{\text{net}} \chi_{d(k)|a(j)}^{\text{net}} \right] \right.$$

$$- \left[\chi_{a(j)|d(k)}^{\text{net}} - \chi_{a(j)}^{\text{loop}}(Y - y_1, |\vec{b} - \vec{b}_1|) \right] \left[\left(1 - e^{-\chi_{d(k)|a(j)}^{\text{net}}} \right) e^{-\chi_{a(j)|d(k)}^{\text{net}}} - \chi_{d(k)|a(j)}^{\text{net}} \right]$$

$$\left. + \chi_{d(k)}^{\mathbb{P}}(y_1, b_1) \left[\chi_{a(j)}^{\text{loop}}(Y - y_1, |\vec{b} - \vec{b}_1|) - \chi_{a(j)}^{\text{loop}(1)}(Y - y_1, |\vec{b} - \vec{b}_1|) \right] \right\}, \quad (22)$$

where $Y = \ln(s/s_0)$ and the omitted arguments of the eikonals read $\chi_{a(j)|d(k)}^{\text{net}} = \chi_{a(j)|d(k)}^{\text{net}}(Y - y_1, \vec{b} - \vec{b}_1 | Y, \vec{b})$, $\chi_{d(k)|a(j)}^{\text{net}} = \chi_{d(k)|a(j)}^{\text{net}}(y_1, \vec{b}_1 | Y, \vec{b})$. As demonstrated in [14], Eqs. (17-22) account for all important enhanced diagram contributions to elastic scattering amplitude.

The generalization of the treatment for nucleus-nucleus scattering amplitude is described in Appendix A.

3 Configurations of final states

The knowledge of the elastic scattering amplitude is far insufficient for the construction of a MC procedure for hadronic and nuclear inelastic collisions. What we need are partial cross sections for particular configurations of final states, which are defined by contributions of the corresponding unitarity cuts of elastic scattering diagrams. Those can be easily derived in the nonenhanced eikonal scheme using the Abramovskii-Gribov-Kancheli (AGK) cutting rules [22]. Considering diagrams with precisely $m \geq 1$ Pomerons being cut, each cut Pomeron corresponding to an elementary production process, and summing over any number of uncut Pomerons which describe additional elastic rescatterings, one obtains the so-called topological cross sections for hadron-hadron scattering [17, 18]:

$$\sigma_{ad}^{(m)}(s) = \int d^2 b \; \sum_{j,k} C_{j/a} C_{k/d} \frac{\left(2\chi_{ad(jk)}^{\mathbb{P}}(s, b) \right)^m}{m!} e^{-2\chi_{ad(jk)}^{\mathbb{P}}(s, b)}. \qquad (23)$$

The integrand in (23) can be interpreted as a probability to have precisely m elementary production processes in the hadron-hadron collision at impact parameter b. On the other hand, combining diagrams where the cut plane passes between $n \geq 2$ Pomerons, none being cut, and choosing either elastic or inelastic states in the cut plane for the projectile and the target, one obtains either elastic σ_{ad}^{el} or various (low mass) diffraction cross sections. For example, for σ_{ad}^{el} and for single projectile hadron diffraction cross section one obtains [17]:

$$\sigma_{ad}^{\text{el}}(s) = \int d^2 b \; \left[\sum_{j,k} C_{j/a} C_{k/d} \left(1 - e^{-\chi_{ad(jk)}^{\mathbb{P}}(s, b)} \right) \right]^2 \qquad (24)$$

7

$$\sigma_{ad}^{\mathrm{SD(proj)}}(s) = \int d^2b \sum_{j,k,l,m} \left(C_{j/a}\,\delta_{jl} - C_{j/a}C_{l/a}\right) C_{k/d}C_{m/d}\; e^{-\chi_{ad(jk)}^{\mathbb{P}}(s,b)-\chi_{ad(lm)}^{\mathbb{P}}(s,b)}. \tag{25}$$

It is worth stressing that a configuration of the final state is defined by the structure of the unitarity cuts, here - by the number of *cut Pomeron* exchanges, and implies a resummation of all absorptive corrections due to virtual rescattering processes - uncut Pomeron exchanges.

Taking into account enhanced Pomeron diagrams significantly complicates the analysis and produces a variety of final state configurations, including e.g. ones with single or multiple large rapidity gaps (LRG) not covered by secondary particle production. The complete set of AGK-based cut enhanced diagrams has been derived in [13], the corresponding contributions being composed of various unitarity cuts of net-fan subgraphs, and contains cut diagrams of two types. The first class consists of cut diagrams characterized by a "tree"-like structure of cuts; such graphs are constructed coupling arbitrary numbers of cut and uncut net-fan contributions in one central (not necessarily unique) vertex, such that each cut net-fan subgraph is characterized by a "fan"-like structure of cuts [13]. The diagrams of the second kind are characterized by a "zigzag"-like structure of cuts; they are constructed in a similar way, with the important difference that at least one of the cut net-fan subgraphs has a zigzaglike structure of cuts, with subsequent Pomeron end rapidities satisfying $y_1 > y_2 < y_3 > \cdots$. Treelike cut diagrams give important contributions to the total cross section and to partial cross sections of various final states; they provide main corrections to inclusive spectra of secondary particles. On the other hand, various contributions of zigzaglike cut graphs to the total cross section precisely cancel each other, moreover, as demonstrated in [14], they do not influence noticeably the rapidity gap structure of final states. Nevertheless, such diagrams provide contributions to inclusive particle spectra and to partial cross sections for particular final states. Therefore, our strategy will be to develop first a MC scheme taking into consideration treelike cut enhanced graphs only. After that, the procedure will be complemented by taking into account zigzaglike cut contributions.

As discussed above, to obtain cross sections for various final state configurations, we shall use as "building blocks" contributions of various unitarity cuts of net-fan graphs. For the moment, we are interested in the AGK-cuts of net-fans, characterized by a fanlike structure of cuts, which are defined by the Schwinger-Dyson equations of Fig. 5 [3] [13, 14]. The top line of the Figure defines the contribution $2\hat{\chi}_{a(j)|d(k)}^{\mathrm{fan}}$ of the subset of graphs in which the Pomeron loop sequence coupled to the vertex (y_1, b_1) (the handle of the fan) is crossed by the cut plane. In turn, the equation in the bottom line gives the one of the diagrams where the handle of the fan remains uncut, $2\tilde{\chi}_{a(j)|d(k)}^{\mathrm{fan}}$. The total contribution of fanlike cuts of net-fans is thus $2\bar{\chi}_{a(j)|d(k)}^{\mathrm{fan}} = 2\hat{\chi}_{a(j)|d(k)}^{\mathrm{fan}} + 2\tilde{\chi}_{a(j)|d(k)}^{\mathrm{fan}}$. The first graph in the r.h.s. of the top line corresponds to all possible AGK-based cuts of the single 2-point sequence of Pomerons and Pomeron loops exchanged between the vertex (y_1, b_1) and the projectile hadron whereas the next two diagrams in the r.h.s. of the graphic equation describe the development of the cut Pomeron net: The vertex (y_2, b_2) couples together $\bar{m} \geq 1$ cut projectile net-fans, each one characterized by a fanlike structure of cuts, and any numbers $m, n \geq 0$ of uncut projectile and target net-fans, such that $\bar{m}+m+n \geq 2$. There one has to subtract the contributions of the next two diagrams which correspond to configurations of non-AGK type, where in all the $\bar{m}$ cut projectile net-fans connected to the vertex (y_2, b_2) the handles of the fans remain uncut and are situated on the same side of the cut plane, together with all the m uncut projectile net-fans. Finally, in the last graph in the top line of the Figure the cut plane passes between $m \geq 2$ uncut projectile net-fans, with at least one remaining on either side of the cut, such that a large rapidity gap is formed between the projectile proton and the vertex (y_2, b_2). The diagrams in the bottom line of the Figure have a similar structure, as discussed in more detail in [13, 14].

---

[3]Here and in the following we use a slightly different graphic notation compared to Figs. 3, 4: a shaded ellipse with solid margins, positioned between the vertices (y_1, b_1) and (y_2, b_2), denotes a general (not necessarily irreducible) 2-point sequence of Pomerons and Pomeron loops exchanged between these vertices, with the corresponding contribution $[1 - \exp(-\chi^{\mathrm{loop}}(y_1 - y_2, |\vec{b}_1 - \vec{b}_2|))]$. Similarly, such an ellipse with dashed margins corresponds to the AGK cuts of such a sequence, with the contribution $2[1 - \exp(-\chi^{\mathrm{loop}}(y_1 - y_2, |\vec{b}_1 - \vec{b}_2|))]$.
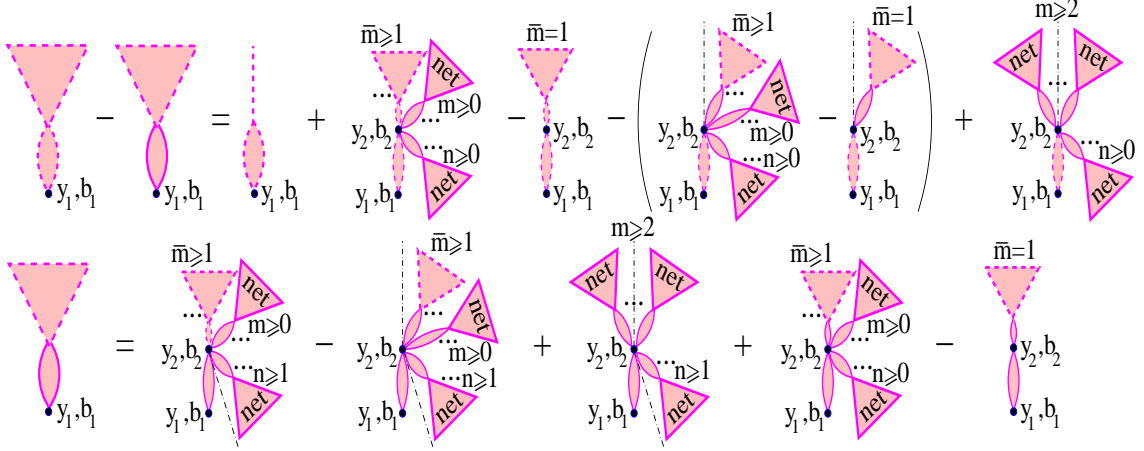
Figure **5**: Recursive representations for cut net-fan diagrams characterized by a fanlike structure of cuts. The top line of the figure defines the contribution $2\hat{\chi}^{\text{fan}}_{a(j)|d(k)}$ of the subset of graphs in which the handle of the fan is cut; the bottom line gives the one of the diagrams with uncut handle, $2\tilde{\chi}^{\text{fan}}_{a(j)|d(k)}$.

As demonstrated in [13], the total contribution of fanlike cuts of net-fans coincides with twice the uncut one:

$$2\bar{\chi}^{\text{fan}}_{a(j)|d(k)}(y_1, \vec{b}_1|Y, \vec{b}) = 2\chi^{\text{net}}_{a(j)|d(k)}(y_1, \vec{b}_1|Y, \vec{b}), \tag{26}$$

whereas for $2\hat{\chi}^{\text{fan}}_{a(j)|d(k)}$ one obtains the recursive equation

$$2\hat{\chi}^{\text{fan}}_{a(j)|d(k)}(y_1, \vec{b}_1|Y, \vec{b}) = 2\chi^{\text{loop}}_{a(j)}(y_1, b_1) + 2G \int_{\xi}^{y_1 - \xi} dy_2 \int d^2 b_2 \left(1 - e^{-\chi^{\text{loop}}(y_1 - y_2, |\vec{b}_1 - \vec{b}_2|)}\right)$$

$$\times \left[\left(1 - e^{-\hat{\chi}^{\text{fan}}_{a(j)|d(k)}(y_2, \vec{b}_2|Y, \vec{b})}\right) e^{-2\chi^{\text{net}}_{d(k)|a(j)}(Y - y_2, \vec{b} - \vec{b}_2|Y, \vec{b})} - \hat{\chi}^{\text{fan}}_{a(j)|d(k)}(y_2, \vec{b}_2|Y, \vec{b})\right]. \tag{27}$$

In Appendix B we derive also alternative representations for $2\hat{\chi}^{\text{fan}}_{a(j)|d(k)}$, $2\tilde{\chi}^{\text{fan}}_{a(j)|d(k)}$ which can be used in a MC procedure to generate the cut Pomeron structure of an irreducible cut diagram, to be discussed in Section 4. In addition, we obtain there subcontributions $2\chi^{\text{loop}}_{a(j)|d(k)}$, $2\tilde{\chi}^{\text{loop}}_{a(j)|d(k)}$, which correspond to such cuts of net-fan graphs in which just one *cut* Pomeron is coupled to hadron a.

Using the above-defined building blocks, the complete set of cut irreducible graphs (with a treelike structure of cuts) for hadron-hadron scattering is given in Fig. 6 [4] [13]. Each square bracket in the Figure corresponds to a positively defined contribution of a certain "macro-configuration" of the final state, characterized by certain topology of *cut* Pomerons, hence, by a definite pattern for secondary hadron production. For example, the diagrams in the first square bracket in Fig. 6 correspond to the configuration with at least two cut projectile and target net-fans ($\bar{m} \geq 2$, $\bar{n} \geq 2$) coupled together in the vertex ($y_1, \vec{b}_1$), which results in a treelike structure of the final state: [5] In each of the $\bar{m}$ cut projectile net-fans any cut Pomeron may split into a few, forming a fanlike structure (composed of cut Pomerons) developing towards the projectile hadron (in the 0s order with respect to the triple-Pomeron coupling a cut net-fan is represented by a single cut Pomeron exchanged between the hadron and the multi-Pomeron vertex); in all the $\bar{n}$ cut target net-fans such fanlike structures develop towards the target hadron. For the corresponding contribution we

---

[4]As discussed in [13], the set of diagrams of Fig. 6 can also be represented in a form explicitly symmetric with respect to the projectile and the target.

[5]The 2nd and 3rd graphs in the square bracket define the subtracted contributions of the cuts of non-AGK types.
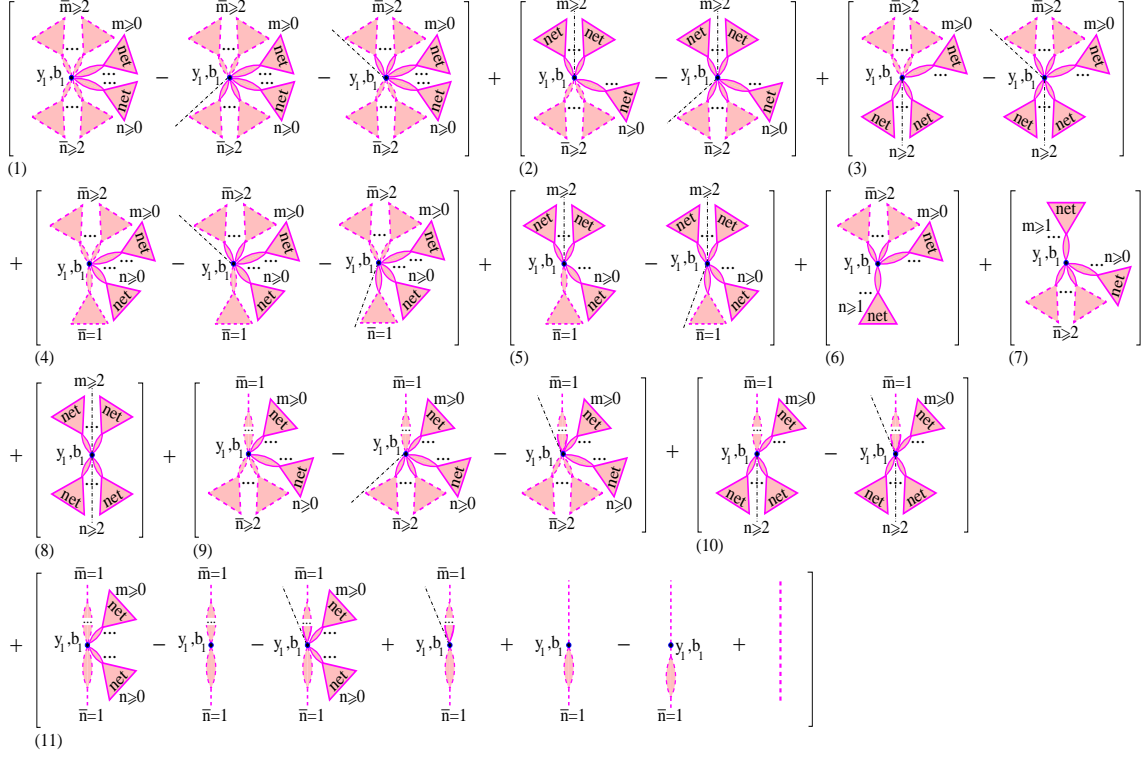
Figure **6**: Complete set of irreducible cut diagrams characterized by a "tree"-like structure of cuts.

obtain

$$\bar{\Omega}^{(1)}_{ad(jk)}(s,b) = \frac{G}{2} \int_{\xi}^{Y-\xi} dy_1 \int d^2 b_1 \sum_{\bar{m}=2}^{\infty} \sum_{\bar{n}=2}^{\infty} \left\{ \frac{\left[2\hat{\chi}^{\mathrm{fan}}_{a(j)|d(k)} + 2\tilde{\chi}^{\mathrm{fan}}_{a(j)|d(k)} \right]^{\bar{m}}}{\bar{m}!} e^{-2\chi^{\mathrm{net}}_{a(j)|d(k)}} \right.$$

$$\times \frac{\left[2\hat{\chi}^{\mathrm{fan}}_{d(k)|a(j)} + 2\tilde{\chi}^{\mathrm{fan}}_{d(k)|a(j)} \right]^{\bar{n}}}{\bar{n}!} e^{-2\chi^{\mathrm{net}}_{d(k)|a(j)}} - 2 \frac{\left[2\hat{\chi}^{\mathrm{fan}}_{a(j)|d(k)} + 2\tilde{\chi}^{\mathrm{fan}}_{a(j)|d(k)} \right]^{\bar{m}}}{\bar{m}!} e^{-2\chi^{\mathrm{net}}_{a(j)|d(k)}}$$

$$\times \frac{\left[\tilde{\chi}^{\mathrm{fan}}_{d(k)|a(j)} \right]^{\bar{n}}}{\bar{n}!} e^{-\chi^{\mathrm{net}}_{d(k)|a(j)}} - 2 \frac{\left[\tilde{\chi}^{\mathrm{fan}}_{a(j)|d(k)} \right]^{\bar{m}}}{\bar{m}!} e^{-\chi^{\mathrm{net}}_{a(j)|d(k)}} \frac{\left[2\hat{\chi}^{\mathrm{fan}}_{d(k)|a(j)} + 2\tilde{\chi}^{\mathrm{fan}}_{d(k)|a(j)} \right]^{\bar{n}}}{\bar{n}!} e^{-2\chi^{\mathrm{net}}_{d(k)|a(j)}} \right\}$$

$$= \frac{G}{2} \int_{\xi}^{Y-\xi} dy_1 \int d^2 b_1 \left\{ \left[1 - e^{-2\chi^{\mathrm{net}}_{a(j)|d(k)}} \left(1 + 2\chi^{\mathrm{net}}_{a(j)|d(k)} \right) \right] \left[1 - e^{-2\chi^{\mathrm{net}}_{d(k)|a(j)}} \left(1 + 2\chi^{\mathrm{net}}_{d(k)|a(j)} \right) \right] \right.$$

$$-2 \left[1 - e^{-2\chi^{\mathrm{net}}_{a(j)|d(k)}} \left(1 + 2\chi^{\mathrm{net}}_{a(j)|d(k)} \right) \right] \left[e^{\tilde{\chi}^{\mathrm{fan}}_{d(k)|a(j)}} - 1 - \tilde{\chi}^{\mathrm{fan}}_{d(k)|a(j)} \right] e^{-\chi^{\mathrm{net}}_{d(k)|a(j)}}$$

$$\left. -2 \left[e^{\tilde{\chi}^{\mathrm{fan}}_{a(j)|d(k)}} - 1 - \tilde{\chi}^{\mathrm{fan}}_{a(j)|d(k)} \right] e^{-\chi^{\mathrm{net}}_{a(j)|d(k)}} \left[1 - e^{-2\chi^{\mathrm{net}}_{d(k)|a(j)}} \left(1 + 2\chi^{\mathrm{net}}_{d(k)|a(j)} \right) \right] \right\}, (28)$$

where the abbreviations are similar to the ones in (22).

The 2nd class of graphs corresponds to a LRG produced (in one particular inelastic rescattering process) between the projectile hadron and the vertex $(y_1, \vec{b}_1)$ and at least two cut target net-fans $(\bar{n} \geq 2)$ coupled to the vertex $(y_1, \vec{b}_1)$, while in the third configuration the projectile and the target

interchange their places. The corresponding contributions read

$$\bar{\Omega}^{(2)}_{ad(jk)}(s,b) = \frac{G}{2} \int_{\xi}^{Y-\xi} dy_1 \int d^2b_1 \left[1 - e^{-\chi^{\text{net}}_{a(j)|d(k)}}\right]^2$$

$$\times \left\{ \left[1 - e^{-2\chi^{\text{net}}_{d(k)|a(j)}} \left(1 + 2\chi^{\text{net}}_{d(k)|a(j)}\right)\right] - 2\left[e^{\tilde{\chi}^{\text{fan}}_{d(k)|a(j)}} - 1 - \tilde{\chi}^{\text{fan}}_{d(k)|a(j)}\right] e^{-\chi^{\text{net}}_{d(k)|a(j)}} \right\} \qquad (29)$$

$$\bar{\Omega}^{(3)}_{ad(jk)}(s,b) = \frac{G}{2} \int_{\xi}^{Y-\xi} dy_1 \int d^2b_1 \left[1 - e^{-\chi^{\text{net}}_{d(k)|a(j)}}\right]^2$$

$$\times \left\{ \left[1 - e^{-2\chi^{\text{net}}_{a(j)|d(k)}} \left(1 + 2\chi^{\text{net}}_{a(j)|d(k)}\right)\right] - 2\left[e^{\tilde{\chi}^{\text{fan}}_{a(j)|d(k)}} - 1 - \tilde{\chi}^{\text{fan}}_{a(j)|d(k)}\right] e^{-\chi^{\text{net}}_{a(j)|d(k)}} \right\}. \qquad (30)$$

The next two contributions are similar to the first pair, with the difference that there is precisely one cut target net-fan ($\bar{n} = 1$) coupled to the vertex $(y_1, \vec{b}_1)$:

$$\bar{\Omega}^{(4)}_{ad(jk)}(s,b) = G \int_{\xi}^{Y-\xi} dy_1 \int d^2b_1 \left\{ \left[1 - e^{-2\chi^{\text{net}}_{a(j)|d(k)}} \left(1 + 2\chi^{\text{net}}_{a(j)|d(k)}\right)\right] \left[\chi^{\text{net}}_{d(k)|a(j)} e^{-2\chi^{\text{net}}_{d(k)|a(j)}} \right. \right.$$

$$\left. - \tilde{\chi}^{\text{fan}}_{d(k)|a(j)} e^{-\chi^{\text{net}}_{d(k)|a(j)}}\right] - 2\left[e^{\tilde{\chi}^{\text{fan}}_{a(j)|d(k)}} - 1 - \tilde{\chi}^{\text{fan}}_{a(j)|d(k)}\right] e^{-\chi^{\text{net}}_{a(j)|d(k)}} \chi^{\text{net}}_{d(k)|a(j)} e^{-2\chi^{\text{net}}_{d(k)|a(j)}} \right\} \quad (31)$$

$$\bar{\Omega}^{(5)}_{ad(jk)}(s,b) = G \int_{\xi}^{Y-\xi} dy_1 \int d^2b_1 \left[1 - e^{-\chi^{\text{net}}_{a(j)|d(k)}}\right]^2 \left[\chi^{\text{net}}_{d(k)|a(j)} e^{-2\chi^{\text{net}}_{d(k)|a(j)}} - \tilde{\chi}^{\text{fan}}_{d(k)|a(j)} e^{-\chi^{\text{net}}_{d(k)|a(j)}}\right]. \quad (32)$$

In the 6th contribution, the secondary particles produced are separated from the target hadron by a LRG which extends beyond the vertex $(y_1, \vec{b}_1)$: In all the $\bar{m} \geq 2$ cut projectile net-fans the handles of the fans are uncut and positioned on the same side of the cut plane, together with all the $m \geq 0$ uncut projectile and $n \geq 1$ target net-fans. In the next graph the projectile and the target interchange their roles, the two contributions being

$$\bar{\Omega}^{(6)}_{ad(jk)}(s,b) = 2G \int_{\xi}^{Y-\xi} dy_1 \int d^2b_1 \left[e^{\tilde{\chi}^{\text{fan}}_{a(j)|d(k)}} - 1 - \tilde{\chi}^{\text{fan}}_{a(j)|d(k)}\right] e^{-\chi^{\text{net}}_{a(j)|d(k)}} \left(1 - e^{-\chi^{\text{net}}_{d(k)|a(j)}}\right) \qquad (33)$$

$$\bar{\Omega}^{(7)}_{ad(jk)}(s,b) = 2G \int_{\xi}^{Y-\xi} dy_1 \int d^2b_1 \left[e^{\tilde{\chi}^{\text{fan}}_{d(k)|a(j)}} - 1 - \tilde{\chi}^{\text{fan}}_{d(k)|a(j)}\right] e^{-\chi^{\text{net}}_{d(k)|a(j)}} \left(1 - e^{-\chi^{\text{net}}_{a(j)|d(k)}}\right). \qquad (34)$$

In the graph in the 8th square bracket, there are only uncut net-fans coupled to the vertex $(y_1, \vec{b}_1)$; particle production emerges here from the cut multi-Pomeron vertex $(y_1, \vec{b}_1)$ only and is separated by large rapidity gaps from both the projectile and the target.[6] For the corresponding contribution we easily obtain

$$\bar{\Omega}^{(8)}_{ad(jk)}(s,b) = \frac{G}{2} \int_{\xi}^{Y-\xi} dy_1 \int d^2b_1 \left[1 - e^{-\chi^{\text{net}}_{a(j)|d(k)}}\right]^2 \left[1 - e^{-\chi^{\text{net}}_{d(k)|a(j)}}\right]^2. \qquad (35)$$

The next set of cut enhanced diagrams reminds the one in the 4th square bracket, being reversed upside-down, with the difference that the vertex $(y_1, \vec{b}_1)$ is coupled to the projectile by a single cut sequence of Pomerons and Pomeron loops, the corresponding contributions $2\bar{\chi}^{\text{loop}}_{a(j)|d(k)}$, $2\tilde{\chi}^{\text{loop}}_{a(j)|d(k)}$ being defined in Appendix B. Thus, the cut Pomeron "tree" develops here towards the target while there is only one cut Pomeron coupled to the projectile. The partial contribution of such a configuration is

$$\bar{\Omega}^{(9)}_{ad(jk)}(s,b) = G \int_{\xi}^{Y-\xi} dy_1 \int d^2b_1 \left\{ \left[\bar{\chi}^{\text{loop}}_{a(j)|d(k)} e^{-2\chi^{\text{net}}_{a(j)|d(k)}} - \tilde{\chi}^{\text{loop}}_{a(j)|d(k)} e^{-\chi^{\text{net}}_{a(j)|d(k)}}\right] \right.$$

$$\times \left[1 - e^{-2\chi^{\text{net}}_{d(k)|a(j)}} \left(1 + 2\chi^{\text{net}}_{d(k)|a(j)}\right)\right] - 2\bar{\chi}^{\text{loop}}_{a(j)|d(k)} e^{-2\chi^{\text{net}}_{a(j)|d(k)}} \left[e^{\tilde{\chi}^{\text{fan}}_{d(k)|a(j)}} - 1 - \tilde{\chi}^{\text{fan}}_{d(k)|a(j)}\right] e^{-\chi^{\text{net}}_{d(k)|a(j)}} \right\}. \quad (36)$$

---

[6]In the following we shall neglect the production of such low mass diffractive states at central rapidities, such that this particular set of diagrams will contribute to (quasi-)elastic rescattering processes only. As demonstrated in [14], such low mass diffractive states produced at central rapidities do not provide significant contributions to diffraction cross sections, with the sole exception of the central diffraction (double Pomeron exchange).

In turn, the next contribution corresponds to a single cut sequence of Pomerons and Pomeron loops, exchanged between the projectile and the vertex $(y_1, \vec{b}_1)$ and being separated from the target by a LRG:

$$\bar{\Omega}^{(10)}_{ad(jk)}(s,b) = G \int_{\xi}^{Y-\xi} dy_1 \int d^2 b_1 \left[\tilde{\chi}^{\text{loop}}_{a(j)|d(k)} \, e^{-2\chi^{\text{net}}_{a(j)|d(k)}} - \tilde{\chi}^{\text{loop}}_{a(j)|d(k)} \, e^{-\chi^{\text{net}}_{a(j)|d(k)}} \right] \left[1 - e^{-\chi^{\text{net}}_{d(k)|a(j)}} \right]^2 . \quad (37)$$

Finally, the graphs in the last square bracket in Fig. 6 describe an exchange of a single cut sequence of Pomerons and Pomeron loops between the projectile and the target hadrons, which includes also a single cut Pomeron exchange, with the contribution

$$\bar{\Omega}^{(11)}_{ad(jk)}(s,b) = 2\chi^{\mathbb{P}}_{ad(jk)}(s,b) + 2G \int_{\xi}^{Y-\xi} dy_1 \int d^2 b_1 \left\{ \chi^{\text{loop}}_{d(k)}(y_1, b_1) \left[\tilde{\chi}^{\text{loop}}_{a(j)|d(k)} \left(e^{-2\chi^{\text{net}}_{a(j)|d(k)} - 2\chi^{\text{net}}_{d(k)|a(j)}} - 1 \right) \right. \right.$$
$$\left. - \, \tilde{\chi}^{\text{loop}}_{a(j)|d(k)} \left(e^{-\chi^{\text{net}}_{a(j)|d(k)} - 2\chi^{\text{net}}_{d(k)|a(j)}} - 1 \right) \right] + \chi^{\mathbb{P}}_{a(j)}(Y - y_1, |\vec{b} - \vec{b}_1|) \left[\chi^{\text{loop}}_{d(k)}(y_1, b_1) - \chi^{\text{loop}(1)}_{d(k)}(y_1, b_1) \right] \right\}. \quad (38)$$

As shown in [13], one has the identity

$$\sum_{i=1}^{11} \bar{\Omega}^{(i)}_{ad(jk)}(s,b) = \Omega_{ad(jk)}(s,b), \quad (39)$$

which relates the summary contribution of all the considered cut diagrams to the total opacity $\Omega_{ad(jk)}$ for hadron-hadron scattering, Eqs. (2), (22). Relation (39) is a direct consequence of the s-channel unitarity of the approach and of the fact that contributions of zigzaglike cut graphs to the elastic scattering amplitude precisely cancel each other [13]. Using (39), we can easily write down the absorptive cross section which corresponds to multiple secondary hadron production, including high mass diffraction processes:

$$\sigma^{\text{abs}}_{ad}(s) = \int d^2 b \sum_{N=1}^{\infty} \frac{\left[\sum_{i=1}^{11} \bar{\Omega}^{(i)}_{ad(jk)}(s,b) \right]^N}{N!} \, e^{-\Omega_{ad(jk)}(s,b)} = \int d^2 b \left[1 - e^{-\Omega_{ad(jk)}(s,b)} \right], \quad (40)$$

where the factor $\left[\sum_{i=1}^{11} \bar{\Omega}^{(i)}_{ad(jk)} \right]^N / N! = \left[\Omega_{ad(jk)} \right]^N / N!$ comes from an exchange of precisely N irreducible cut graphs whereas the factor $\exp\left[-\Omega_{ad(jk)} \right]$ is obtained summing over any number (≥ 0) of elastic rescattering processes due to the exchanges of uncut graphs. Proceeding as in Appendix A, the treatment can be generalized to the case of nucleus-nucleus (hadron-nucleus) collisions, as outlined in Appendix C.

It is noteworthy that total inelastic cross section contains also contributions from low mass diffraction of the projectile and/or target hadrons:

$$\sigma^{\text{inel}}_{ad}(s) = \sigma^{\text{abs}}_{ad}(s) + \sigma^{\text{SD(proj)}}_{ad}(s) + \sigma^{\text{SD(targ)}}_{ad}(s) + \sigma^{\text{DD}}_{ad}(s), \quad (41)$$

where the latter are defined as [cf. (25)]

$$\sigma^{\text{SD(proj)}}_{ad}(s) = \int d^2 b \sum_{j,k,l,m} (C_{j/a}\,\delta_{jl} - C_{j/a}C_{l/a})\, C_{k/d}C_{m/d}\, e^{-\frac{1}{2}\Omega_{ad(jk)}(s,b) - \frac{1}{2}\Omega_{ad(lm)}(s,b)} \quad (42)$$

$$\sigma^{\text{SD(targ)}}_{ad}(s) = \int d^2 b \sum_{j,k,l,m} C_{j/a}C_{l/a}(C_{k/d}\,\delta_{km} - C_{k/d}C_{m/d})\, e^{-\frac{1}{2}\Omega_{ad(jk)}(s,b) - \frac{1}{2}\Omega_{ad(lm)}(s,b)} \quad (43)$$

$$\sigma^{\text{DD}}_{ad}(s) = \int d^2 b \sum_{j,k,l,m} (C_{j/a}\,\delta_{jl} - C_{j/a}C_{l/a})\,(C_{k/d}\,\delta_{km} - C_{k/d}C_{m/d})\, e^{-\frac{1}{2}\Omega_{ad(jk)}(s,b) - \frac{1}{2}\Omega_{ad(lm)}(s,b)}. \quad (44)$$

Eqs. (40-44) form the basis for a MC treatment of inelastic hadron-hadron collisions. In particular, using Eq. (40), for a given geometrical configuration of the collision (impact parameter $\vec{b}$ and elastic scattering eigenstates j and k of the projectile and target hadrons) the factor $\left[\Omega_{ad(jk)}\right]^N / N! \, \exp\left[-\Omega_{ad(jk)}\right]$ can be interpreted as the probability for precisely N elementary inelastic interactions to take place in the collision. Each of the elementary interactions may have different topologies (defined by the structure of the unitarity cuts) of the kinds discussed above, characterized by partial probabilities $\bar{\Omega}_{ad(jk)}^{(i)} / \Omega_{ad(jk)}$. It is worth stressing that the probabilistic interpretation of Eq. (40) and the positive-definiteness of the partial cut contributions $\bar{\Omega}_{ad(jk)}^{(i)}$ are due to the full resummation of absorptive corrections due to virtual rescattering processes, in particular, due to the resummation of all the irreducible cut diagrams characterized by a given topology of the cuts, with any number of uncut Pomerons and any number of multi-Pomeron vertices.

4 Monte Carlo procedure

The obtained expressions allow a relatively straightforward MC implementation of the approach, which is discussed below for the case of hadron-hadron scattering. While low mass diffraction processes, being sampled according to the corresponding probabilities $\sigma_{ad}^{\mathrm{SD(proj)}}/\sigma_{ad}^{\mathrm{inel}}$, $\sigma_{ad}^{\mathrm{SD(targ)}}/\sigma_{ad}^{\mathrm{inel}}$, and $\sigma_{ad}^{\mathrm{DD}}/\sigma_{ad}^{\mathrm{inel}}$ [Eqs. (42)-(44)], are treated like in the original QGSJET model [3, 21] - assuming the $\mathbb{PPR}$-asymptotics for the mass distribution of diffractive states, the "true inelastic" interactions, which have the partial probability $\sigma_{ad}^{\mathrm{abs}}/\sigma_{ad}^{\mathrm{inel}}$, are simulated as follows. One starts from sampling the squared impact parameter for the collision - uniformly in the area $b^2 < b_{\mathrm{max}}^2$, with b_{max} chosen sufficiently large, corresponding to negligibly small interaction probability at $b > b_{max}$. In addition, one generates elastic scattering eigenstates j and k for the projectile and target hadrons - according to their partial weights $C_{j/a}$, $C_{k/d}$. In the specified geometry, one defines the number $N \geq 0$ of elementary inelastic processes according to the Poisson distribution with the mean $\Omega_{ad(jk)}$ - Eq. (40); in case $N = 0$ the chosen geometry is rejected and the above-discussed steps are repeated.

Next, for each of the N elementary production processes one chooses first the "macro-structure" of the contributing cut diagrams (as defined in Fig. 6) - according to the positively-defined weights $\bar{\Omega}_{ad(jk)}^{(i)} / \Omega_{ad(jk)}$, and reconstructs the configuration of cut Pomerons for the corresponding set of irreducible cut graphs. For example, for the macro-configuration of the 1st square bracket in Fig. 6 one chooses the rapidity y_1 and transverse vector $\vec{b}_1$ of the central multi-Pomeron vertex $(y_1, \vec{b}_1)$ - according to the integrand of Eq. (28), and samples the numbers of cut projectile and target net-fans $\bar{m}$, $\bar{n}$ using the Poisson distribution with the corresponding mean values $2\chi_{a(j)|d(k)}^{\mathrm{net}}$, $2\chi_{d(k)|a(j)}^{\mathrm{net}}$ (rejecting the cases $\bar{m}, \bar{n} < 2$) - see the 1st term in the integrand of Eq. (28). For each of the $\bar{m}$ cut projectile net-fans one decides if the handle of the fan is cut - with the probability $\hat{\chi}_{a(j)|d(k)}^{\mathrm{fan}} / \chi_{a(j)|d(k)}^{\mathrm{net}}$, or uncut (similarly for the $\bar{n}$ cut target net-fans); the 2nd and 3rd terms in the integrand of Eq. (28) are accounted for via rejection in the case all the $\bar{m}$ cut projectile net-fans and/or the $\bar{n}$ cut target net-fans have their handles uncut. After that, the cut Pomeron structure for each of the $\bar{m} + \bar{n}$ cut net-fans is reconstructed using an iterative procedure, as discussed in Appendix D. By the end of the procedure one is left with cut Pomeron contributions of three types: i) stretched between the projectile and target hadrons; ii) between a given (projectile or target) hadron and a certain multi-Pomeron vertex; iii) between a pair of multi-Pomeron vertices.

Each of those cut Pomeron contributions corresponds to an underlying elementary parton cascade developing in the respective rapidity range; hadronization of partons results in the production of secondary hadrons which densely fill that rapidity interval. For example, a cut Pomeron exchanged between the projectile and the target hadrons gives rise to particle production in the whole

range $[0, Y]$.[7]A cut Pomeron exchanged between, say, projectile hadron and some multi-Pomeron vertex $(y', \vec{b}')$ results in a chain of secondaries covering the range $[y', Y]$, etc. It is noteworthy that we speak here about cut Pomeron contributions in the sense of Fig. 23, i.e. accounting also for absorptive corrections for the corresponding configuration of the final state: The cut Pomeron contribution includes also the ones of diagrams with additional multi-Pomeron vertices placed along the cut Pomeron line; those vertices are coupled to *uncut* Pomerons which are in turn connected to the projectile and/or the target and/or to other uncut Pomerons.

Certain configurations obtained may contain large rapidity gaps not covered by secondary particles - when the corresponding rapidity intervals are not spanned by any cut Pomeron. For example, in the configuration of Fig. 7, cut Pomerons cover rapidity intervals $[y_1, y_2]$, $[y_3, y_4]$,
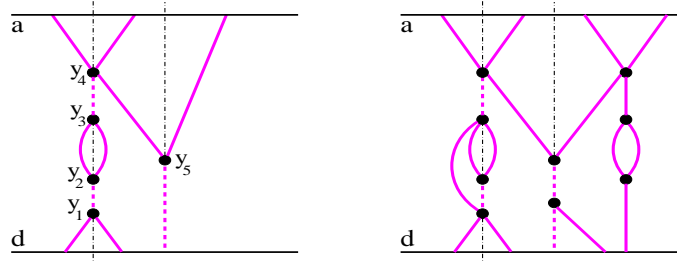
Figure **7**: Example of a cut enhanced graph corresponding to a final state with two LRGs (left) and a more complicated graph which describes absorptive corrections to the same final state (right).

and $[0, y_5]$, resulting in the production of chains of secondary particles in those rapidity ranges. Hence, LRGs are produced in the intervals $[y_5, y_3]$ and $[y_4, Y]$. On the other hand, there is no rapidity gap in the interval $[0, y_1]$ which is covered by secondaries emerging from the rightmost cut Pomeron in the graph. While the diagram in Fig. 7 (left) is the simplest one corresponding to the discussed final state, the one in Fig. 7 (right) illustrates some absorptive corrections to the discussed configuration, which are accounted for by the formalism.

In addition to the already generated configuration, which is based on treelike cut enhanced graphs, an additional set of cut Pomerons comes from zigzaglike cut diagrams. The latter are treated using an effective procedure, as outlined in Appendix E.

At the next step, both for the projectile and the target hadrons one performs energy-momentum sharing between all the constituent partons (Pomeron ends) connected to them and generates inelastic excitations of the remaining remnant states. Finally, for each cut Pomeron contribution, either exchanged between the projectile and the target, or between a given (projectile or target) hadron and a multi-Pomeron vertex, or between a pair of multi-Pomeron vertices, one chooses whether it is represented by its soft or semihard Pomeron component. In the latter case, like in the nonenhanced Pomeron scheme [3, 19], one samples the light cone momenta for the "leg"-partons of the QCD ladder and performs simulation of the development of the corresponding perturbative parton cascade. One employs the standard treatment to reconstruct the pattern of both initial and final state parton emission using the forward evolution algorithms described in [19]. One ends up with the formation of strings stretched between the Pomeron end-point partons in case of soft Pomerons; for semihard Pomerons such strings are stretched also between the final s-channel partons resulted from the perturbative cascades, following the direction of the color flow.

The treatment is completed with the fragmentation of strings into secondary hadrons, which is performed using the original procedure of the QGSJET model [21], using the algorithm described in [23], with string fragmentation parameters expressed via intercepts of secondary Regge trajectories [24].

---

[7]Constituent partons ("Pomeron ends") are characterized by a relatively hard light cone momentum distribution, hence, no LRGs arise from the energy-momentum partition between those partons and the hadron "remnant" state.
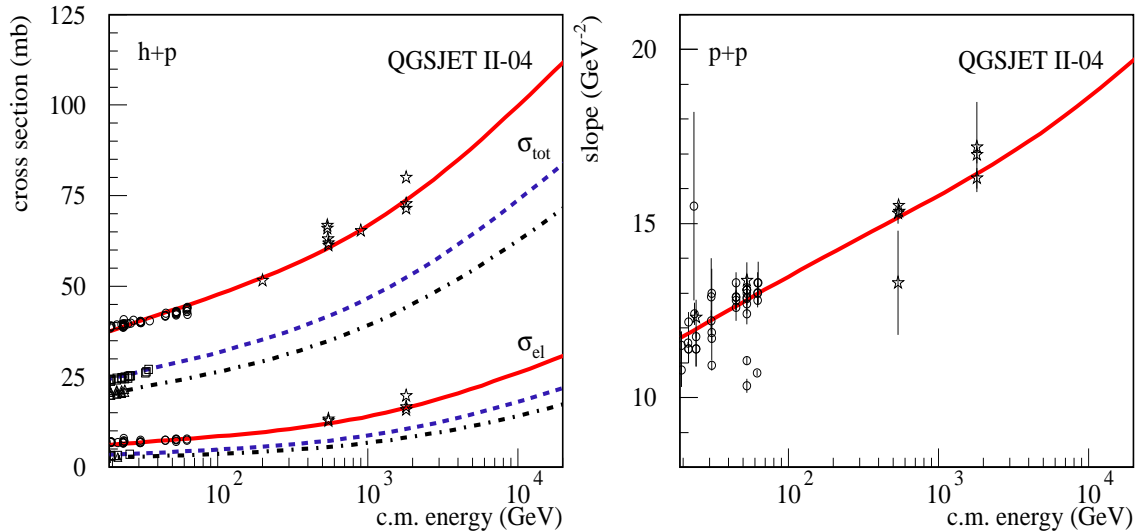
Figure **8**: Left: Calculated total and elastic proton-proton, pion-proton, and kaon-proton cross sections - respectively solid, dashed, and dotted-dashed lines. Right: Calculated elastic scattering slope for proton-proton scattering. The compilation of experimental data (points) is from Ref. [25].

5   Some results and discussion

The basic model parameters have been calibrated from the combined description of total and elastic hadron-proton cross sections, elastic scattering slopes, and total and diffractive structure functions F_2, $F_2^{\mathrm{D}(3)}$, the latter two being calculated as described in [20], generalizing the corresponding expressions to account also for Pomeron loop contributions. In turn, the parameters for the hadronization procedure have been tuned comparing with data on hadron production in proton-proton interactions, using also new data sets obtained at the Large Hadron Collider.

Using the virtuality cutoff $Q_0^2 = 3$ GeV^2 between the soft and hard parton evolution, we obtained in particular for the soft Pomeron intercept and slope $\alpha_{\mathbb{P}} = 1.17$, $\alpha_{\mathbb{P}}' = 0.11$, while for the triple-Pomeron coupling we got $r_{3\mathbb{P}} = 0.1$ GeV, with $\gamma_{\mathbb{P}} = 0.4$ GeV^{-1}. The corresponding results for $\sigma_{hp}^{\mathrm{tot}}(s)$, $\sigma_{hp}^{\mathrm{el}}(s)$, $B_{pp}^{\mathrm{el}}(s)$, $d\sigma_{hp}^{\mathrm{el}}(s,t)/dt$, and for proton structure function $F_2(x,Q^2)$ are given in Figs. 8, 9, 10 in comparison with experimental data. Using the simple exponential form (6) for the t-dependence of hadronic form factors, the calculated differential elastic cross sections agree reasonably well with measurements at small $|t| \lesssim 0.3$ GeV^2 which are responsible for the bulk of secondary hadron production. To have a better agreement at larger values of $|t|$, a dipole parametrization for the form factor would be more suitable.

In Fig. 11, we compare the calculated proton diffractive structure function $F_2^{\mathrm{D}(3)}(x, x_{\mathbb{P}}, Q^2)$ (proton dissociation excluded) for small Q^2, $x_{\mathbb{P}}$, $\beta = x/x_{\mathbb{P}}$ with HERA data. Our interest to this observable is related to its strong sensitivity to the main parameter for the enhanced Pomeron scheme – the triple-Pomeron coupling. It is easy to see that the model results for $F_2^{\mathrm{D}(3)}$ agree with the measurements only in the limit of small Q^2, $x_{\mathbb{P}}$, and β. With increasing $x_{\mathbb{P}}$, the $\mathbb{RRP}$ contribution to $F_2^{\mathrm{D}(3)}$ becomes important while for larger β and Q^2 so-called $q\bar{q}$ diffractive component (multiple Pomeron coupling to the $q\bar{q}$-loop) has to be accounted for [35], both contributions neglected in the present treatment.[8] Thus, diffractive HERA data set the *upper limit* on the value of the triple-Pomeron vertex.

In Fig. 12 we plot the obtained energy dependence for single and double diffractive proton-proton cross sections in comparison to CDF data [36, 37], showing also partial contributions of high

---

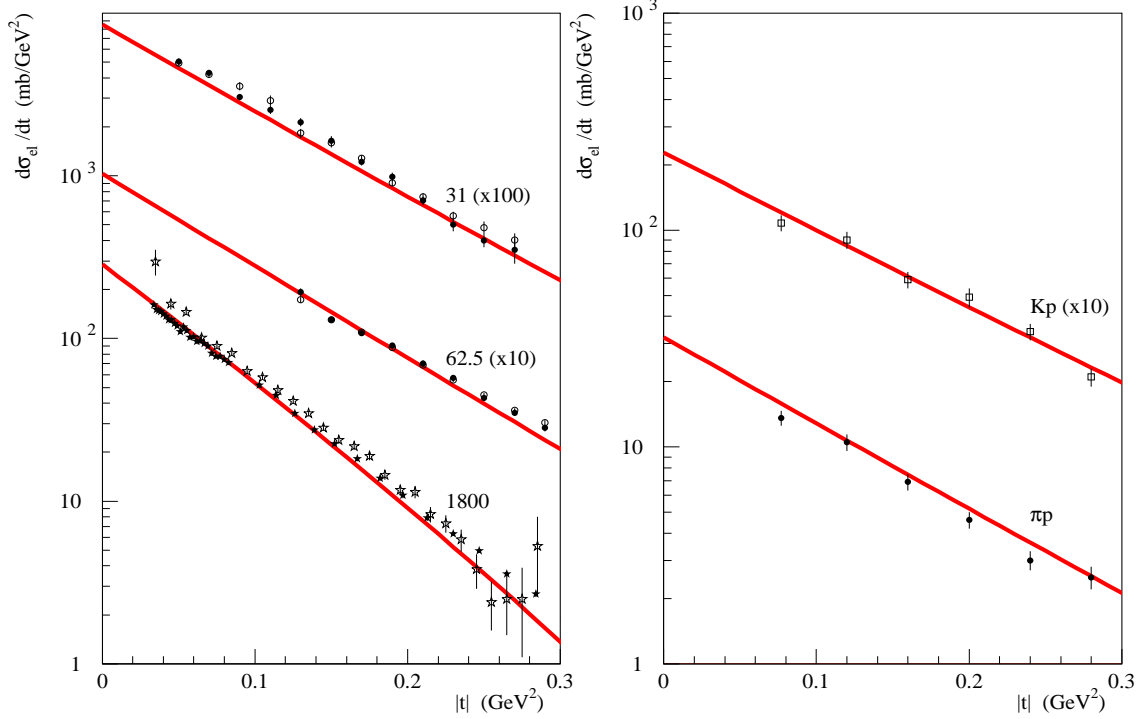[8]Neither of the two neglected contributions involves the triple-Pomeron coupling.

Figure **9**: Left: Calculated differential elastic proton-proton cross section for different $\sqrt{s}$ in GeV (as indicated in the plot). Right: Calculated differential elastic pion-proton and kaon-proton cross sections for the projectile lab. momentum 250 GeV/c. Experimental data are from Refs. [26, 27, 28, 29, 30, 31].
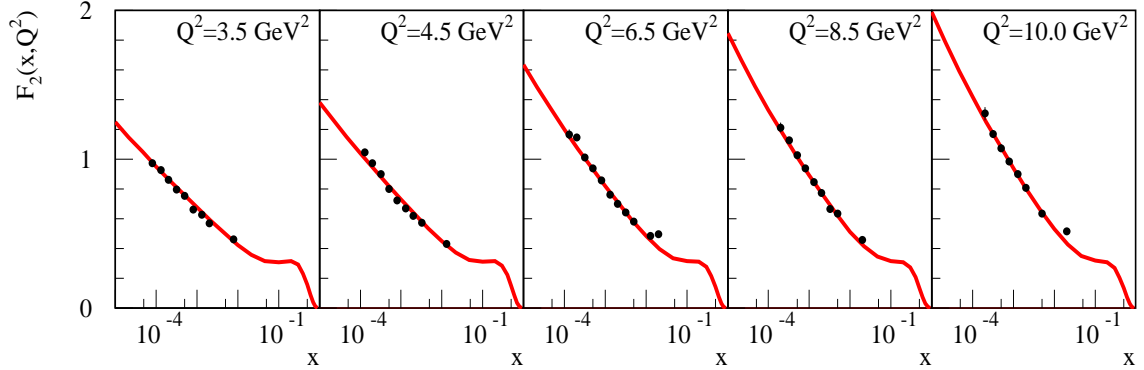

Figure **10**: Calculated proton structure function $F_2(x, Q^2)$ compared to HERA data [32].

mass diffractive states to the discussed cross sections and the contribution of high mass diffraction of one proton and a low mass excitation of the other one. Here we adopt the experimental definitions for the diffractive cross sections, applying the respective event selection triggers to hadronic final states generated via a MC procedure: Single diffraction events are obtained when either a projectile or target proton is separated from the remaining final state of mass M_X by a LRG and $M_X^2/s < 0.15$ [36]; double diffraction events contain a central rapidity gap of size $y_{\text{gap}} \geq 3$, which spans the central rapidity $y = \ln s/2$ point [37]. Diffractive states are classified as high mass ones when $M_X^2 > 25$ GeV^2 and as low mass excitations otherwise [36]. It is noteworthy that at comparatively
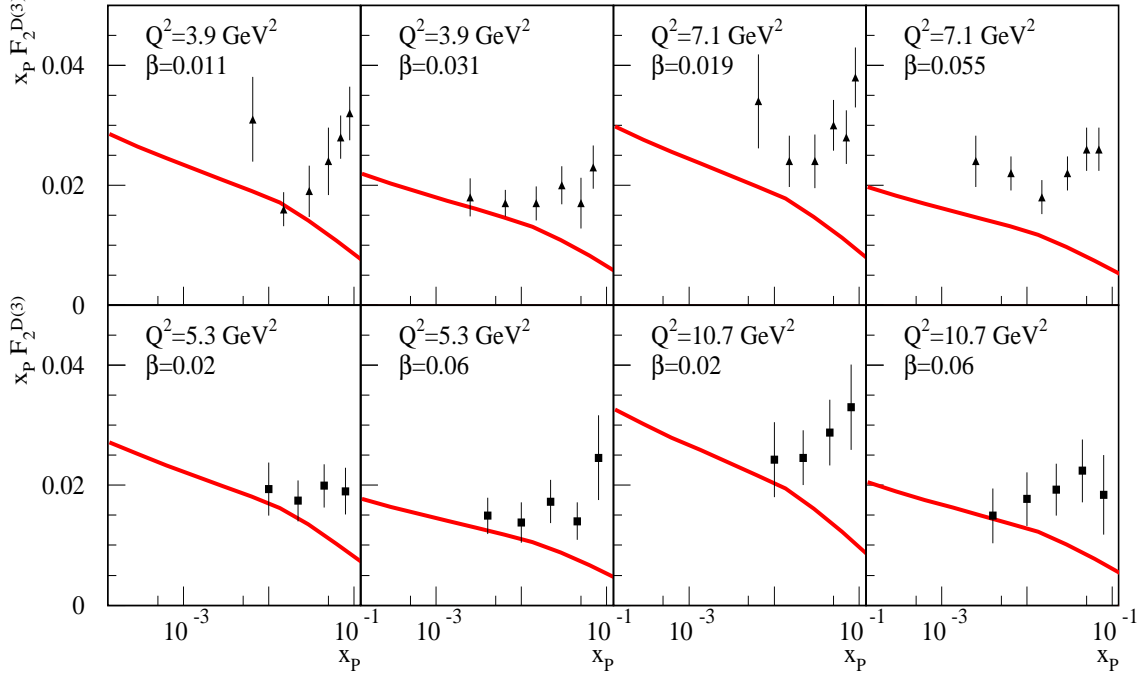
16

Figure **11**: Calculated proton diffractive structure function $F_2^{D(3)}(x, x_{\mathbb{P}}, Q^2)$ compared to ZEUS [33] (triangles) and H1 [34] (squares) data.
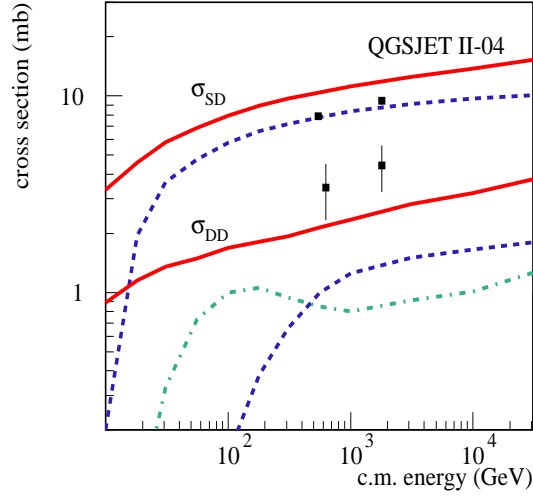

Figure **12**: Calculated single $\sigma_{pp}^{\text{SD}}(M_X^2/s < 0.15)$ and double $\sigma_{pp}^{\text{DD}}(y_{\text{gap}}^{(0)} \geq 3)$ diffraction proton-proton cross sections (solid lines), compared to CDF data (points) [36, 37]; high mass diffraction contributions to σ_{pp}^{SD}, σ_{pp}^{DD} (dashed lines); contribution to σ_{pp}^{DD} from a high mass diffraction of one proton and a low mass excitation of the other one (dotted-dashed line).

low energies ($\sqrt{s} \sim 10$ GeV) certain (theoretically) nondiffractive final states satisfy the imposed triggers, constituting about half of the plotted σ_{pp}^{SD} and most of the σ_{pp}^{DD}. On the other hand, at sufficiently high energies a part of the theoretical low mass diffraction, being described by the $\mathbb{P}\mathbb{P}\mathbb{R}$-asymptotics, is classified as high mass diffraction, which explains the energy dependence of

17

the "low-high" double diffraction cross section (dotted-dashed line in Fig. 12). The obtained values for σ_{pp}^{SD} agree reasonably well with the measurements, taking the fact that most of the low mass diffraction contribution could not be seen by the CDF detector [36]. In turn, double diffraction is seriously underestimated by the model.

A comparison with selected data on secondary particle production in proton-proton and proton-antiproton collisions, which have been used for the model calibration, is presented in Figs. 13, 14, 15. In Figs. 13 and 14 the calculated Feynman x spectra of protons and charged pions as well as
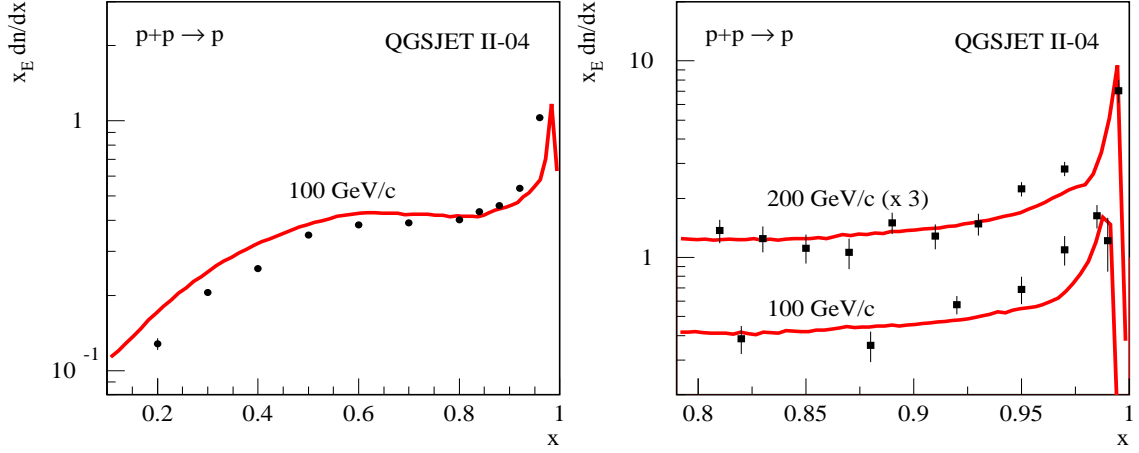

Figure **13**: Calculated Feynman x spectra of secondary protons in proton-proton collisions at 100 and 200 GeV/c lab. momentum compared to data from Refs. [38] (circles) and [39] (squares).
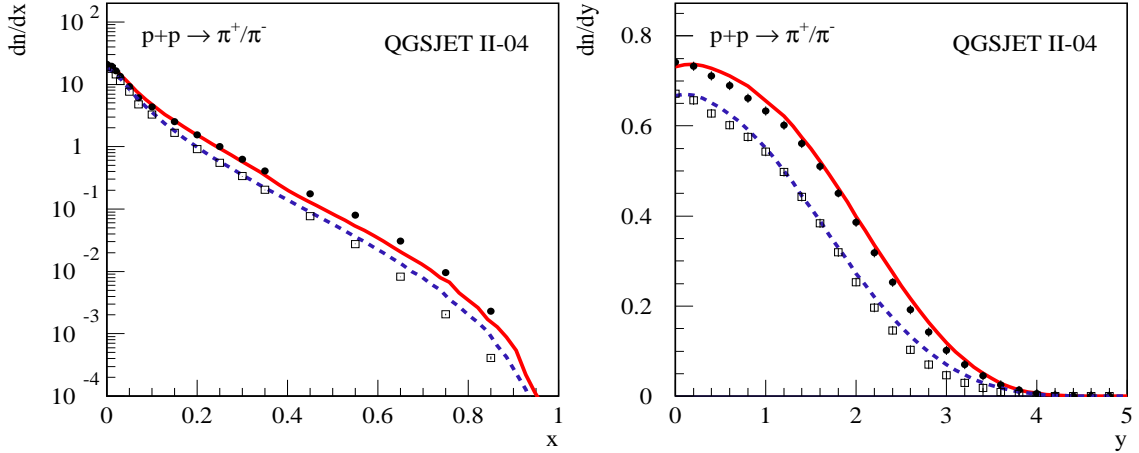

Figure **14**: Calculated Feynman x spectra (left) and rapidity distributions (right) of positive (solid lines) and negative (dashed lines) pions in proton-proton collisions at 158 GeV/c lab. momentum compared to NA49 data [40].

pion rapidity distributions are plotted together with data from fixed target experiments. In turn, Fig. 15 shows the results of calculations of the pseudorapidity density and of transverse momentum spectra of charged secondaries in non-single-diffractive (NSD) proton-antiproton and proton-proton collisions over a broad range of energies $\sqrt{s} = 0.2 \div 7$ TeV in comparison with experimental data from the $Sp\bar{p}S$, Tevatron, and LHC colliders.[9] More extensive compilation of the model results for

---

[9]The calculations have been performed using the NSD triggers of the respective experiments.
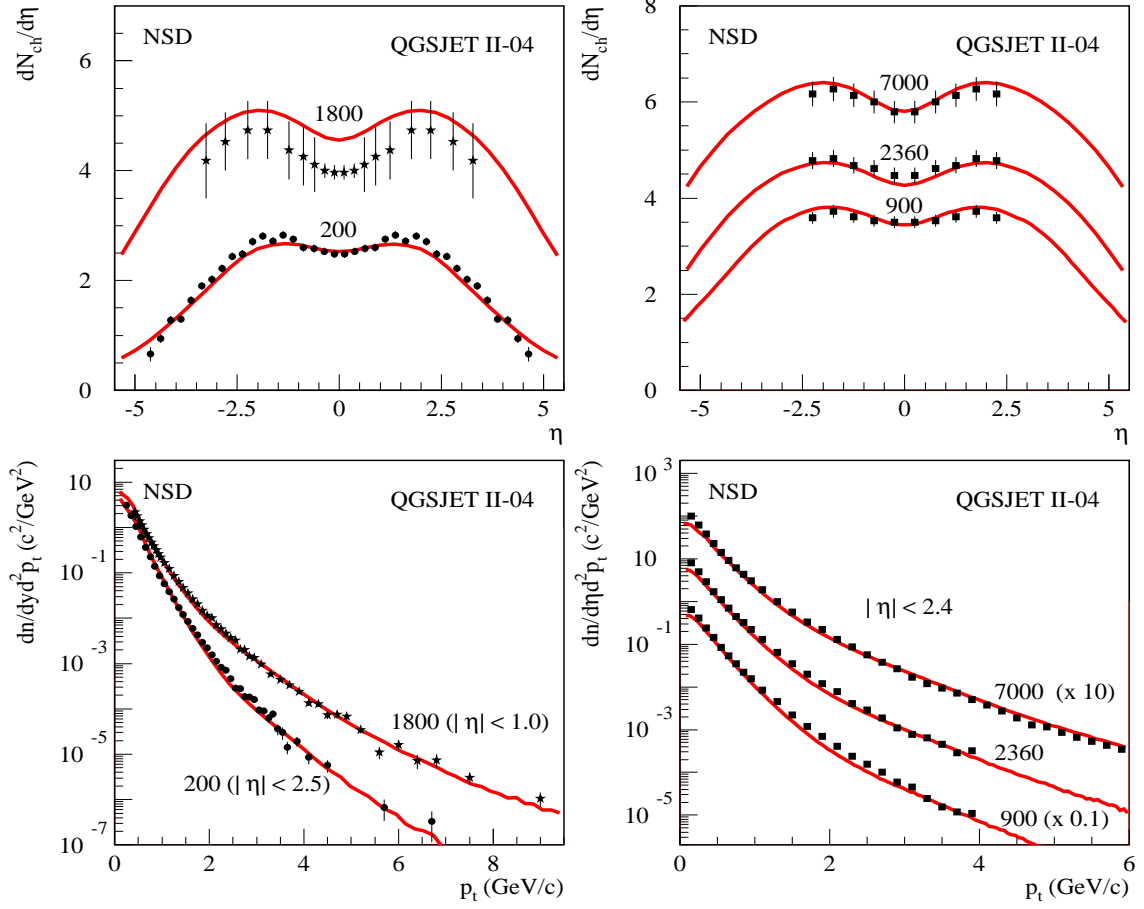
18

Figure **15**: Calculated pseudorapidity density (top row) and transverse momentum spectra (bottom row) of charged particles produced in proton-antiproton (left panels) and proton-proton (right panels) collisions at different c.m. energies in GeV (as indicated in the plots). The data points are from Refs. [41, 42, 43, 44, 45].

secondary particle production will be presented elsewhere [15].

An interesting potential test for hadronic interaction models, which could be performed using particle detectors at the LHC, has been proposed in Ref. [46]. The idea was to compare event trigger rates obtained by LHC experiments, using different combinations of the respective charged particle scintillation counters. As such counters cover a restricted range of pseudorapidities, $\eta_1 < |\eta| < \eta_2$, with $\eta_1 = 3.1$, $\eta_2 = 6.5$ for the TOTEM detector [47] and $\eta_1 = 2$, $\eta_2 = 4$ for ATLAS [48], the so-called minimum-bias trigger (MBT) selections by the experiments will miss a significant fraction of the inelastic proton-proton cross section, which will include both the low mass diffraction and a part of the high mass one. Using various combinations of such triggers, one gains sensitivity both to the absolute value of $\sigma_{pp}^{\mathrm{inel}}$ and to the contributions of single and double high mass diffraction, which have different selection efficiencies by such triggers. In Table 1 we present our predictions for trigger rates by the TOTEM and ATLAS experiments at $\sqrt{s} = 14$ TeV, in comparison to the original calculations of Ref. [46], for the selection of triggers proposed in that work: requiring a charge particle hit at positive rapidities only (in the interval $[\eta_1, \eta_2]$ covered by scintillators) - MBT1, or a signal at either positive ($[\eta_1, \eta_2]$) or negative ($[-\eta_2, -\eta_1]$) rapidities - MBT2, or with both detectors being fired - MBT3. The calculated trigger rates for the presently attained LHC energy $\sqrt{s} = 7$ TeV are collected in Table 2. Comparing our results with those of Ref. [46], we

	σ_{tot}	σ_{inel}	TOTEM			ATLAS		
			σ_{MBT1}	σ_{MBT2}	σ_{MBT3}	σ_{MBT1}	σ_{MBT2}	σ_{MBT3}
this work	105	76.8	66.6	69.7	63.4	63.9	66.4	61.3
[46]	91.5	70.0	50.7	59.0	42.4	46.6	50.8	42.4

Table **1**: Calculated total, inelastic and minimum-bias (for different MBT selections) proton-proton cross sections at $\sqrt{s} = 14$ TeV.

σ_{tot}	σ_{inel}	TOTEM			ATLAS		
		σ_{MBT1}	σ_{MBT2}	σ_{MBT3}	σ_{MBT1}	σ_{MBT2}	σ_{MBT3}
93.3	69.7	60.8	64.3	57.4	58.1	60.8	55.3

Table **2**: Same as in Table 1 for $\sqrt{s} = 7$ TeV.

observe large differences concerning both the absolute magnitude of the calculated minimum-bias cross sections and for their variations between different trigger selections. Although such differences are partly due to hadronization effects - as we apply the respective triggers to hadronic final states generated via a MC procedure, the largest effect is related to a considerably higher total (hence, also inelastic) cross section and to a much smaller (by a factor of 2) single high mass diffraction cross section in our approach compared to [46], as discussed in more detail in [14]. Nevertheless, the discussed triggers work in a similar way for both model approaches, particularly for the MBT selections of ATLAS: i) all the three triggers reject low mass diffraction; ii) the MBT3 trigger misses also most of single high mass diffraction events; iii) the MBT1 trigger rejects most of the target high mass diffraction. As a consequence, the ratio $(\sigma_{\text{MBT2}} - \sigma_{\text{MBT3}})/(\sigma_{\text{MBT2}} - \sigma_{\text{MBT1}})$ is close to 2. Thus, the present study confirms that the method proposed in [46] will provide a powerful selection between different model approaches to the treatment of minimum-bias hadronic collisions.

As discussed above, the model generalization to hadron-nucleus and nucleus-nucleus collisions does not involve any additional parameters. As an illustration, we plot in Fig. 16 the calculated
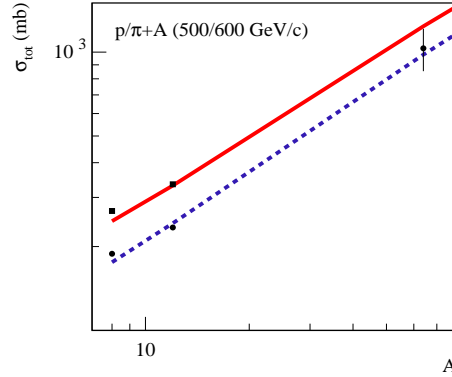

Figure **16**: Calculated A-dependence of total proton-nucleus (solid) and pion-nucleus (dashed) cross sections at respectively 500 and 600 GeV/c lab. momentum compared to experimental data [49].

A-dependence of total hadron-nucleus cross sections in comparison with experimental data. In addition, in Fig. 17 the calculated Feynman x spectra and rapidity distributions of secondary pions in proton-carbon collisions are compared to NA49 data [50].

As demonstrated earlier in [12, 20], the high energy behavior of hadronic cross sections is strongly affected by nonlinear interaction effects. A similarly strong effect is observed when study-
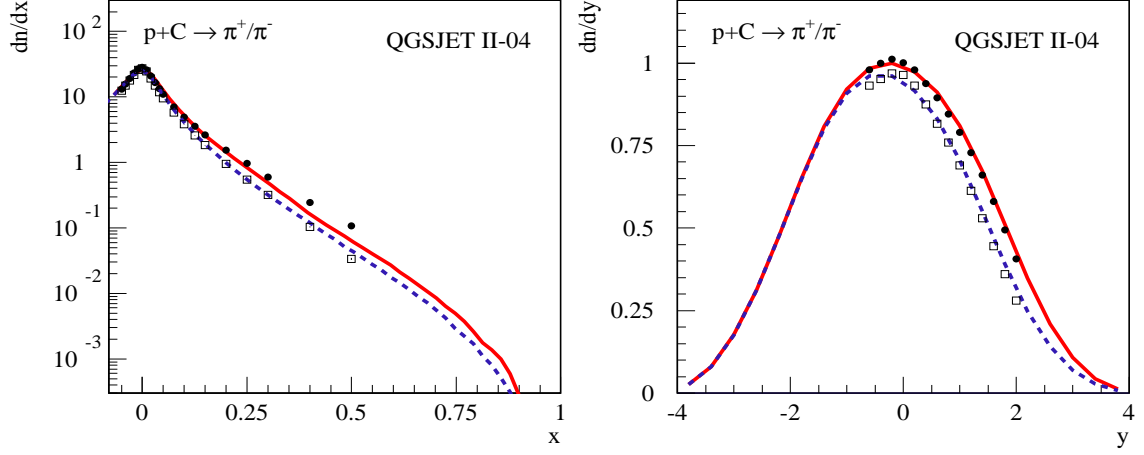
Figure **17**: Calculated Feynman x spectra (left) and rapidity distributions (right) of positive (solid lines) and negative (dashed lines) pions in proton-carbon collisions at 158 GeV/c lab. momentum compared to experimental data [50].

ing the generated configurations for hadronic final states. For proton-proton collisions, we plot in Fig. 18 the energy dependence of the number of "elementary pieces" of secondary production - cut
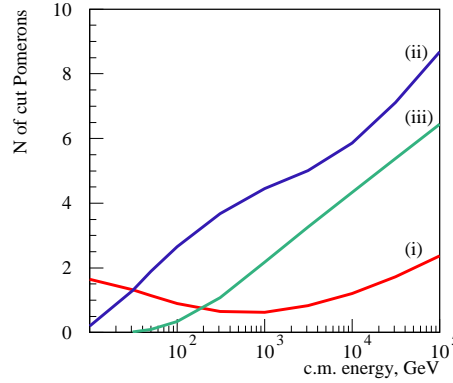

Figure **18**: Energy dependence of the number of cut Pomerons of different types for proton-proton interactions: exchanged between the projectile and target protons (i), exchanged between the projectile or target proton and some multi-Pomeron vertex (ii), exchanged between a pair of multi-Pomeron vertices (iii).

Pomerons, for the three possible contributions: i) cut Pomerons exchanged between the projectile and target protons - which arise from eikonal Pomeron exchanges and obtain absorptive corrections from various cut enhanced graphs characterized by the same pattern of the final state; ii) ones exchanged between the projectile or target proton and some multi-Pomeron vertex - which come from cut enhanced graphs only (see the examples of the corresponding subgraphs in Fig. 23); iii) cut Pomerons exchanged between a pair of multi-Pomeron vertices. While at moderately low energies the configuration of the interaction is dominated by cut Pomerons of the first type - as one would have in a (linear) eikonal Pomeron scheme, at higher energies the corresponding contribution is damped by absorptive corrections and secondary hadron production comes mainly from the other two contributions - which originate from cut enhanced graphs, i.e. from the treatment of nonlinear interactions. The physical picture behind the observed trend is obvious: The contributions of the

1st kind correspond to a number of elementary parton cascades developing independently between the projectile and target protons and hadronizing into secondary hadrons. With the energy increasing, a large number of such cascades is closely packed together in the phase space, which forces them to overlap and to interact with each other. Thus, production of single chains of secondaries covering the available rapidity range $[0, Y]$ is strongly reduced by virtual (elastic) rescattering of intermediate partons off the projectile and target hadrons. More typical become configurations of fan (or more complicated, see Fig. 6) types, which correspond to multiple *inelastic* rescattering of some intermediate partons off the projectile and target hadrons, leading to a splitting or fusion of the cut Pomeron lines, hence, to a branching of the chains of secondaries and, generally, to a production of large rapidity gaps.

Let us finally stress that the complete all-order resummation of the contributions of all significant enhanced diagrams performed in this work was absolutely necessary for obtaining a self-consistent description of hadronic cross sections and of particle production in the very high energy limit. This is related to the fact that in the high energy asymptotics the diagrams of the highest considered order with respect to Pomeron-Pomeron coupling (more precisely, the ones with the maximal number of Pomerons exchanged in parallel in some rapidity interval) dominate the elastic scattering amplitude [51]. Moreover, proceeding from one order to the next, one obtains sign-changing contributions. Thus, breaking the series at some given order, one obtains the total cross section which either falls down steeply above some energy or starts to rise in a powerlike way, violating the unitarity bound. Hence, a meaningful answer can only be obtained after a resummation of the complete (infinite) series of diagrams. In fact, the situation is even more demanding when applied to calculations of partial cross sections for various (e.g. diffractive) hadronic final states – as different unitarity cuts of the same enhanced graphs give positive contributions to some processes while providing (negative) screening corrections to others. The simplest example of the kind is the triple-Pomeron diagram which provides a steeply rising contribution to high mass single diffraction cross section and gives rise to a strong screening correction to the single cut Pomeron cross section, the latter corresponding to a single elementary production process. An extensive analysis of such effects has been reported in the previous work [14], where also the relative importance of various classes of enhanced diagrams has been investigated.

A comment is in order on the adopted ansatz (10) for multi-Pomeron vertices and on the respective parameter $\gamma_{\mathbb{P}}$. As discussed already in [10, 11] and more recently in [14], in a scheme based on a single Pomeron type, one is forced to choose $\gamma_{\mathbb{P}}$ such that $r_{3\mathbb{P}}/\gamma_{\mathbb{P}} < \Delta_{\mathbb{P}}$ – in order to preserve the energy rise of the scattering amplitude. In the present scheme, apart from the usual soft Pomeron we have also the "semihard Pomeron" contribution [Eqs. (7), (13), (16)] which contains a perturbative "piece". In addition, we assume that multi-Pomeron coupling is dominated by low-q^2 processes ($|q^2| < Q_0^2$), i.e. such vertices are coupled only to soft Pomerons or to soft "ends" of semihard Pomerons,[10] as discussed in more detail in [19, 20]. This allows us to choose $\gamma_{\mathbb{P}}$ such that $r_{3\mathbb{P}}/\gamma_{\mathbb{P}} > \Delta_{\mathbb{P}}$, which leads to a saturation of soft processes in the dense limit (small b and large s) and to a flattening of PDFs *at the input scale* Q_0^2 [52]. The energy rise of the scattering amplitude is supported at very high energies by the increase of the semihard contribution. However, neglecting hard ($|q^2| > Q_0^2$) Pomeron-Pomeron coupling, we are forced to choose the Q_0 cutoff high enough – in order to safely neglect parton saturation effects at $|q^2| > Q_0^2$.[11] This in turn restricts our choice for the parameter $\gamma_{\mathbb{P}}$: For very small $\gamma_{\mathbb{P}}$, in particular, in the limit of triple-Pomeron vertices only ($\gamma_{\mathbb{P}} \to 0$), having the triple-Pomeron coupling $r_{3\mathbb{P}}$ fixed by diffraction data, the saturation of the soft particle production would be achieved at relatively low energies over a large range of impact parameters. As the semihard contribution is still inefficient there, this leads to an underestimation of secondary particle production and to a contradiction with observations. Whether or not one can restrict himself with just the triple-Pomeron vertices can be investigated in the complete scheme

---

[10]The corresponding "hard piece" is always "sandwiched" between a pair of soft Pomerons – see Eqs. (7), (13), (16) and the 2nd graph in the r.h.s. of Fig. 2.

[11]Note that for our choice of the factorization scale $M_{\mathrm{F}}^2 = p_t^2/4$ in Eq. (9) the chosen cutoff corresponds to the minimal transverse momentum in parton hard process $p_{\perp}^{\min} = 2Q_0 \simeq 3.4$ GeV.

only: Taking perturbative Pomeron-Pomeron coupling into consideration.

6   Conclusions

In this paper, we discussed in detail the MC procedure for modeling hadronic collisions in the RFT framework, including the contributions of enhanced Pomeron diagrams. The principal difference of the presented Monte Carlo model compared to other generators of hadronic interactions is the direct correspondence between the RFT treatment and the MC implementation: Various hadronic final states are generated according to their partial cross sections. The latter are defined by the contributions of cut Pomeron diagrams characterized by the relevant structure of the cuts. Defining the contributions of certain cut subgraphs by means of recursive equations, we were able to generate the (generally complicated) structure of hadronic final states in an iterative fashion.

The described model represents a self-consistent implementation of the corresponding RFT treatment, providing, in particular, a close link between the description of total and elastic hadron-proton cross sections and the generation of hadronic final states. Indeed, while the elastic scattering amplitude is defined by the contributions of uncut nonenhanced and enhanced diagrams, partial cross sections for various final states are defined by unitarity cuts of the very same diagrams, the summary contribution of all the cuts being related to the uncut one by s-channel unitarity [Eqs. (39), (84)], as demonstrated explicitly in [13]. On the other hand, the generalization of the treatment to hadron-nucleus and nucleus-nucleus case, both concerning cross section calculations and for modeling particle production, does not involve additional adjustable parameters.

Being based on the RFT formalism, the present treatment shares most of its usual assumptions, like the validity of the AGK cutting rules and eikonal vertices for Pomeron-hadron (Pomeron-Pomeron) coupling. It also has the usual drawback of neglecting energy-momentum correlations between multiple scattering processes at the amplitude level [53]. Thus, the discussed model remains a phenomenological one and it is experimental data which have to decide if it is suitable enough for the treatment of very high energy hadronic collisions. While in the current work we mainly addressed the construction of the MC generator and showed only some representative results for secondary particle spectra, a thorough comparison of the model predictions on particle production with available experimental data and the model applications for air shower simulation will be presented elsewhere [15].

Appendix A

The generalization of the approach described in Section 2 to hadron-nucleus and nucleus-nucleus collisions is parameter free and formally straightforward. Indeed, the only essential difference is that now different Pomerons in a given irreducible enhanced graph may couple to different nucleons of the projectile and/or target nuclei, whose positions in the impact parameter plane should be chosen according to the corresponding nuclear density profiles. Thus, in case of nucleus A - nucleus B interaction, the net-fan contribution (17) should be generalized to

$$\chi_{A|B}^{\text{net}}(y_1, \vec{b}_1 | Y, \vec{b}) = \sum_{m=1}^{A} \chi_{p(j_m^A)}^{\text{loop}}(y_1, |\vec{b}_1 - \vec{b}_m^A|) + G \int_{\xi}^{y_1 - \xi} dy_2 \int d^2 b_2 \left(1 - e^{-\chi^{\text{loop}}(y_1 - y_2, |\vec{b}_1 - \vec{b}_2|)} \right)$$
$$\times \left[\left(1 - e^{-\chi_{A|B}^{\text{net}}(y_2, \vec{b}_2 | Y, \vec{b})} \right) e^{-\chi_{B|A}^{\text{net}}(Y - y_2, \vec{b} - \vec{b}_2 | Y, \vec{b})} - \chi_{A|B}^{\text{net}}(y_2, \vec{b}_2 | Y, \vec{b}) \right], \quad (45)$$

where y_1 is the rapidity distance between the given multi-Pomeron vertex and the nucleus A, $\vec{b}_1$ - the position of the vertex with respect to the center of the nucleus in the transverse plane, j_m^A - elastic scattering eigenstate of m-th nucleon, and $\vec{b}_m^A$ - its transverse vector with respect to the center of the nucleus. Thus, $\chi_{A|B}^{\rm net}$ depends on the positions $\{\vec{b}^A, \vec{b}^B\}$ and the elastic scattering eigenstates $\{j^A, k^B\}$ of all the $A + B$ nucleons of the interacting nuclei, the corresponding indexes not shown explicitly in (45). The general contribution of irreducible enhanced graphs is generalized in a similar way:

$$\chi_{AB}^{\rm enh}(s, b, \{j^A, k^B, \vec{b}^A, \vec{b}^B\}) = G \int_\xi^{Y-\xi} dy_1 \int d^2 b_1 \left\{ \left[\left(1 - e^{-\chi_{A|B}^{\rm net}} \right) \left(1 - e^{-\chi_{B|A}^{\rm net}} \right) - \chi_{A|B}^{\rm net} \chi_{B|A}^{\rm net} \right] \right.$$

$$- \left[\chi_{A|B}^{\rm net} - \sum_{m=1}^A \chi_{p(j_m^A)}^{\rm loop}(Y - y_1, |\vec{b} - \vec{b}_1 + \vec{b}_m^A|) \right] \left[\left(1 - e^{-\chi_{B|A}^{\rm net}} \right) e^{-\chi_{A|B}^{\rm net}} - \chi_{B|A}^{\rm net} \right]$$

$$\left. + \sum_{m=1}^A \sum_{n=1}^B \chi_{p(k_n^B)}^{\mathbb{P}}(y_1, |\vec{b}_1 - \vec{b}_n^B|) \left[\chi_{p(j_m^A)}^{\rm loop}(Y - y_1, |\vec{b} - \vec{b}_1 + \vec{b}_m^A|) - \chi_{p(j_m^A)}^{\rm loop(1)}(Y - y_1, |\vec{b} - \vec{b}_1 + \vec{b}_m^A|) \right] \right\}, \quad (46)$$

where the abbreviations are similar to the ones in (22).

It is obvious that Eqs. (45-46) are impractical: for each particular configuration of the two nuclei, i.e. for each choice of the coordinates and elastic scattering eigenstates of the nucleons, one has to calculate $\chi_{A|B}^{\rm net}$ recursively, which is very time-consuming. Unlike hadron-hadron case, one can not make a pretabulation of the corresponding contributions which now depend on $2(A + B)$ coordinates of the nucleons, not counting the numbers of their possible eigenstates and the variables shown explicitly in (45).

To propose a suitable approximation for (45-46) let us decompose $\chi_{A|B}^{\rm net}$ as

$$\chi_{A|B}^{\rm net}(y_1, \vec{b}_1 | Y, \vec{b}) = \sum_{m=1}^A \chi_{p(j_m^A)}^{\rm net}(y_1, |\vec{b}_1 - \vec{b}_m^A|, \cdots), \quad (47)$$

with the aim to describe the dependence of $\chi_{p(j_m^A)}^{\rm net}$ on the coordinates and eigenstates of all the $A+B-1$ projectile and target nucleons but the current one, indicated symbolically by the multidot in the r.h.s. of (47), by means of a single factor. Substituting (47) to (45) and using the identity

$$1 - \exp\left(-\sum_{m=1}^A \chi_{p(j_m^A)}^{\rm net} \right) = \sum_{m=1}^A \left(1 - e^{-\chi_{p(j_m^A)}^{\rm net}} \right) e^{-\sum_{l=1}^{m-1} \chi_{p(j_l^A)}^{\rm net}}, \quad (48)$$

we obtain

$$\sum_{m=1}^A \chi_{p(j_m^A)}^{\rm net}(y_1, |\vec{b}_1 - \vec{b}_m^A|, \cdots)$$

$$= \sum_{m=1}^A \left\{ \chi_{p(j_m^A)}^{\rm loop}(y_1, |\vec{b}_1 - \vec{b}_m^A|) + G \int_\xi^{y_1-\xi} dy_2 \int d^2 b_2 \left(1 - e^{-\chi^{\rm loop}(y_1-y_2, |\vec{b}_1-\vec{b}_2|)} \right) \right.$$

$$\times \left. \left[\left(1 - e^{-\chi_{p(j_m^A)}^{\rm net}(y_2, |\vec{b}_2 - \vec{b}_m^A|, \cdots)} \right) Z_{A|B}^{(m)}(y_2, \vec{b}_2, Y, \vec{b}, \{j^A, k^B, \vec{b}^A, \vec{b}^B\}) - \chi_{p(j_m^A)}^{\rm net}(y_2, |\vec{b}_2 - \vec{b}_m^A|, \cdots) \right] \right\} \quad (49)$$

$$Z_{A|B}^{(m)}(y_2, \vec{b}_2, Y, \vec{b}, \{j^A, k^B, \vec{b}^A, \vec{b}^B\})$$

$$= \exp\left[-\sum_{l=1}^{m-1} \chi_{p(j_l^A)}^{\rm net}(y_2, |\vec{b}_2 - \vec{b}_l^A|, \cdots) - \sum_{n=1}^B \chi_{p(k_n^B)}^{\rm net}(Y - y_2, |\vec{b} - \vec{b}_2 + \vec{b}_n^B|, \cdots) \right]. \quad (50)$$

24

Now we approximate the nuclear screening factor $Z_{A|B}^{(m)}$ for m-th projectile nucleon by its value in the vertex $(y_1, \vec{b}_1)$:

$$Z_{A|B}^{(m)}(y_2, \vec{b}_2, Y, \vec{b}, \{j^A, k^B, \vec{b}^A, \vec{b}^B\}) \simeq Z_{A|B}^{(m)}(y_1, \vec{b}_1, Y, \vec{b}, \{j^A, k^B, \vec{b}^A, \vec{b}^B\}) \,. \tag{51}$$

Using this approximation, the solution of the nuclear net-fan equation (45) is

$$\chi_{A|B}^{\mathrm{net}}(y_1, \vec{b}_1 | Y, \vec{b}) = \sum_{m=1}^{A} \chi_{p(j_m^A)}^{\mathrm{net}}(y_1, |\vec{b}_1 - \vec{b}_m^A|, Z_{A|B}^{(m)}(y_1, \vec{b}_1, Y, \vec{b}, \{j^A, k^B, \vec{b}^A, \vec{b}^B\})) \,, \tag{52}$$

where a partial contribution $\chi_{p(j)}^{\mathrm{net}}$ of any of the A projectile nucleons is the solution of the recursive equation [c.f. (17)]:

$$\chi_{p(j)}^{\mathrm{net}}(y_1, b', Z) = \chi_{p(j)}^{\mathrm{loop}}(y_1, b') + G \int_{\xi}^{y_1 - \xi} dy_2 \int d^2 b_2 \left(1 - e^{-\chi^{\mathrm{loop}}(y_1 - y_2, |\vec{b}' - \vec{b}_2|)}\right)$$
$$\times \left[\left(1 - e^{-\chi_{p(j)}^{\mathrm{net}}(y_2, \vec{b}_2, Z)}\right) Z - \chi_{p(j)}^{\mathrm{net}}(y_2, \vec{b}_2, Z)\right], \tag{53}$$

which can be easily tabulated as a function of its three arguments (y_1, b', Z).

Substituting now (52) to (46) and using (48), we obtain

$$\chi_{AB}^{\mathrm{enh}}(s, b, \{j^A, k^B, \vec{b}^A, \vec{b}^B\}) = \sum_{m=1}^{A} \sum_{n=1}^{B} \chi_{mn}^{\mathrm{enh}}(s, b, \{j^A, k^B, \vec{b}^A, \vec{b}^B\}) \tag{54}$$

$$\chi_{mn}^{\mathrm{enh}}(s, b, \{j^A, k^B, \vec{b}^A, \vec{b}^B\}) = G \int_{\xi}^{Y-\xi} dy_1 \int d^2 b_1 \left\{\left[\left(1 - e^{-\chi_{p(j_m^A)}^{\mathrm{net}}}\right)\left(1 - e^{-\chi_{p(k_n^B)}^{\mathrm{net}}}\right)\right.\right.$$
$$\times e^{-\sum_{l=1}^{m-1} \chi_{p(j_l^A)}^{\mathrm{net}} - \sum_{i=1}^{n-1} \chi_{p(k_i^B)}^{\mathrm{net}}} - \chi_{p(j_m^A)}^{\mathrm{net}} \chi_{p(k_n^B)}^{\mathrm{net}}\right] - \left[\chi_{p(j_m^A)}^{\mathrm{net}} - \chi_{p(j_m^A)}^{\mathrm{loop}}(Y - y_1, |\vec{b} - \vec{b}_1 + \vec{b}_m^A|)\right]$$
$$\times \left[\left(1 - e^{-\chi_{p(k_n^B)}^{\mathrm{net}}}\right) e^{-\sum_{l=1}^{A} \chi_{p(j_l^A)}^{\mathrm{net}} - \sum_{i=1}^{n-1} \chi_{p(k_i^B)}^{\mathrm{net}}} - \chi_{p(k_n^B)}^{\mathrm{net}}\right]$$
$$\left. + \chi_{p(k_n^B)}^{\mathbb{P}}(y_1, |\vec{b}_1 - \vec{b}_n^B|) \left[\chi_{p(j_m^A)}^{\mathrm{loop}}(Y - y_1, |\vec{b} - \vec{b}_1 + \vec{b}_m^A|) - \chi_{p(j_m^A)}^{\mathrm{loop}(1)}(Y - y_1, |\vec{b} - \vec{b}_1 + \vec{b}_m^A|)\right]\right\}, \tag{55}$$

where the omitted arguments read $\chi_{p(k_n^B)}^{\mathrm{net}} = \chi_{p(k_n^B)}^{\mathrm{net}}(y_1, |\vec{b}_1 - \vec{b}_n^B|, Z_{B|A}^{(n)}(y_1, \vec{b}_1, Y, \vec{b}, \{k^B, j^A, \vec{b}^B, \vec{b}^A\}))$, $\chi_{p(j_m^A)}^{\mathrm{net}} = \chi_{p(j_m^A)}^{\mathrm{net}}(Y - y_1, |\vec{b} - \vec{b}_1 + \vec{b}_m^A|, Z_{A|B}^{(m)}(Y - y_1, \vec{b} - \vec{b}_1 + \vec{b}_m^A, Y, \vec{b}, \{j^A, k^B, \vec{b}^A, \vec{b}^B\}))$.

Nucleus-nucleus elastic scattering amplitude $f_{AB}(s, b)$ can now be defined taking into account contributions from any number of Pomerons exchanged between an arbitrary pair of the projectile and target nucleons and from exchanges of arbitrary enhanced graphs between the two nuclei:

$$f_{AB}(s, b) = i \left\langle\left\langle 1 - e^{-\sum_{m=1}^{A} \sum_{n=1}^{B} \chi_{pp(j_m^A k_n^B)}^{\mathbb{P}}(s, |\vec{b} + \vec{b}_m^A - \vec{b}_n^B|) - \chi_{AB}^{\mathrm{enh}}(s, b, \{j^A, k^B, \vec{b}^A, \vec{b}^B\})} \right\rangle_A\right\rangle_B$$

$$= i \left\langle\left\langle 1 - \exp\left[-\frac{1}{2} \sum_{m=1}^{A} \sum_{n=1}^{B} \Omega_{AB}^{(mn)}(s, b, \{j^A, k^B, \vec{b}^A, \vec{b}^B\})\right] \right\rangle_A\right\rangle_B \tag{56}$$

$$\Omega_{AB}^{(mn)}(s, b, \{j^A, k^B, \vec{b}^A, \vec{b}^B\}) = 2\chi_{pp(j_m^A k_n^B)}^{\mathbb{P}}(s, |\vec{b} + \vec{b}_m^A - \vec{b}_n^B|) + 2\chi_{mn}^{\mathrm{enh}}(s, b, \{j^A, k^B, \vec{b}^A, \vec{b}^B\}), \tag{57}$$

where for averaging over transverse coordinates and elastic scattering eigenstates of the nucleons we used the notation

$$\left\langle h(\{j^A, \vec{b}^A\})\right\rangle_A = \sum_{j_1^A \ldots j_A^A} C_{j_1^A/p} \times \ldots \times C_{j_A^A/p} \int d^2 b_1^A \ldots d^2 b_A^A \, T_A(\vec{b}_1^A, \ldots, \vec{b}_A^A) \, h_{j_1^A \ldots j_A^A}(\vec{b}_1^A, \ldots, \vec{b}_A^A) \,,$$

with the profile function T_A being expressed via nuclear ground state density ρ_A as

$$T_A(\vec{b}_1^A, \ldots, \vec{b}_A^A) = \int dz_1^A \ldots dz_A^A \, \rho_A(\vec{r}_1^A, \ldots, \vec{r}_A^A). \tag{58}$$

Expression (57) for nucleus-nucleus scattering amplitude reminds the usual multichannel eikonal form [21], looking as a combination of binarylike nucleon-nucleon rescatterings. In reality, each of the partial opacities $\Omega_{AB}^{(mn)}$ generally depends on the transverse coordinates and elastic scattering eigenstates of all the $A + B$ projectile and target nucleons and contains absorptive corrections due to rescattering processes on those nucleons.

Knowing the elastic amplitude, one can easily calculate total and elastic cross sections as

$$\sigma_{AB}^{\text{tot}}(s) = 2 \int d^2b \, \mathfrak{Im} f_{AB}(s, b) \tag{59}$$

$$\sigma_{AB}^{\text{el}}(s) = \int d^2b \, |f_{AB}(s, b)|^2. \tag{60}$$

Hadron-nucleus scattering amplitude is obtained using in (55-57) $A = 1$, $T_A(\vec{b}_1^A) = \delta^{(2)}(\vec{b}_1^A)$ and replacing the eikonals $\chi_{pp(j_1^A k_n^B)}^{\mathbb{P}}$, $\chi_{p(j_1^A)}^{\text{net}}$ with $\chi_{ap(j_1^A k_n^B)}^{\mathbb{P}}$, $\chi_{a(j_1^A)}^{\text{net}}$ for a given projectile hadron a; the hadron-hadron case is recovered similarly.

Appendix B

To develop a MC procedure for sampling various configurations of hadronic collisions we shall need alternative representations for the cut net-fan contributions $2\hat{\chi}_{a(j)|d(k)}^{\text{fan}}$, $2\tilde{\chi}_{a(j)|d(k)}^{\text{fan}}$. Those should allow us to generate recursively the cut Pomeron structure for the corresponding subgraphs, with all the absorptive corrections due to uncut Pomerons being summed up. Such representations are obtained applying recursively the graphic equations of Fig. 5 to generate a t-channel sequence of multi-Pomeron vertices $(y_2, \vec{b}_2), (y_3, \vec{b}_3), \cdots$, such that these vertices are coupled to uncut projectile and target net-fans only ($m_l + n_l \geq 1$, $\bar{m}_l = \bar{n}_l = 0$, $l = 2, 3, \cdots$) and they are connected to each other by either cut or uncut 2-point sequences of Pomerons and Pomeron loops. The recursive procedure stops in some vertex (y', b') when: i) the vertex (y', b') is connected to the given (here, projectile) hadron by a *cut* 2-point loop sequence, with a single *cut* Pomeron coupled to the hadron, or ii) the vertex is coupled to $\bar{m}' \geq 2$ *cut* projectile net-fans, or iii) the vertex is coupled to $m' \geq 2$ uncut projectile net-fans, with the cut plane positioned between them, i.e. there is a diffractive cut between the projectile hadron and that vertex.[12] The resulting Schwinger-Dyson equations are depicted in Figs. 19, 20 and read

$$2\hat{\chi}_{a(j)|d(k)}^{\text{fan}}(y_1, \vec{b}_1|Y, \vec{b}) = \left[2\bar{\chi}_{a(j)|d(k)}^{\text{loop}}(y_1, \vec{b}_1|Y, \vec{b}) - 2\tilde{\chi}_{a(j)|d(k)}^{\text{loop}}(y_1, \vec{b}_1|Y, \vec{b}) \right] + G \int_\xi^{y_1-\xi} dy' \int d^2b'$$

$$\times \left\{ \left[\chi_{a(j)|d(k)}^{\text{loop}_{\text{cc}}}(y_1, y', \vec{b}_1, \vec{b}'|Y, \vec{b}) \, e^{-2\chi_{d(k)|a(j)}^{\text{net}}} - \chi_{a(j)|d(k)}^{\text{loop}_{\text{cu}}}(y_1, y', \vec{b}_1, \vec{b}'|Y, \vec{b}) \left(1 - e^{-\chi_{d(k)|a(j)}^{\text{net}}} \right) e^{-\chi_{d(k)|a(j)}^{\text{net}}} \right] \right.$$

$$\times \left[\sum_{\bar{m}'=2}^\infty \frac{1}{\bar{m}'!} \left(\left(2\hat{\chi}_{a(j)|d(k)}^{\text{fan}} + 2\tilde{\chi}_{a(j)|d(k)}^{\text{fan}} \right)^{\bar{m}'} e^{-2\chi_{a(j)|d(k)}^{\text{net}}} - 2 \left(\tilde{\chi}_{a(j)|d(k)}^{\text{fan}} \right)^{\bar{m}'} e^{-\chi_{a(j)|d(k)}^{\text{net}}} \right) \right.$$

$$\left. + \left(1 - e^{-\chi_{a(j)|d(k)}^{\text{net}}} \right)^2 \right] - 2\chi_{a(j)|d(k)}^{\text{loop}_{\text{cu}}}(y_1, y', \vec{b}_1, \vec{b}'|Y, \vec{b}) \, e^{-\chi_{a(j)|d(k)}^{\text{net}} - \chi_{d(k)|a(j)}^{\text{net}}} \sum_{\bar{m}'=2}^\infty \frac{\left(\tilde{\chi}_{a(j)|d(k)}^{\text{fan}} \right)^{\bar{m}'}}{\bar{m}'!} \right\} \tag{61}$$

$$2\tilde{\chi}_{a(j)|d(k)}^{\text{fan}}(y_1, \vec{b}_1|Y, \vec{b}) = 2\tilde{\chi}_{a(j)|d(k)}^{\text{loop}}(y_1, \vec{b}_1|Y, \vec{b}) + G \int_\xi^{y_1-\xi} dy' \int d^2b'$$

---

[12]Note, however, that the corresponding rapidity gap may be filled by particles resulting from other cut Pomerons produced in the corresponding rapidity interval.
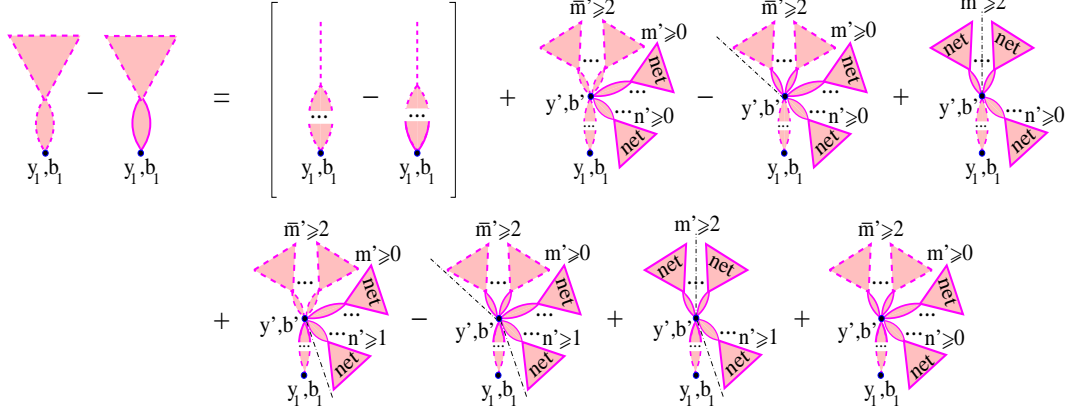
Figure **19**: Alternative representation for the contribution $2\hat{\chi}^{\text{fan}}_{a(j)|d(k)}$ of fanlike cuts of net-fans, the handle of the fan being cut.
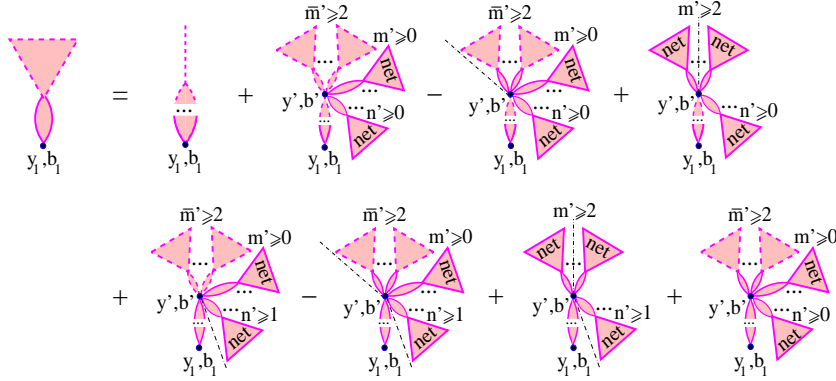

Figure **20**: Alternative representation for the contribution $2\tilde{\chi}^{\text{fan}}_{a(j)|d(k)}$ of fanlike cuts of net-fans, the handle of the fan being uncut.

$$\times \left\{ \left[\chi^{\text{loop}_{\text{uc}}}_{a(j)|d(k)}(y_1, y', \vec{b}_1, \vec{b}'|Y, \vec{b})\, e^{-2\chi^{\text{net}}_{d(k)|a(j)}} + \chi^{\text{loop}_{\text{uu}}}_{a(j)|d(k)}(y_1, y', \vec{b}_1, \vec{b}'|Y, \vec{b}) \left(1 - e^{-\chi^{\text{net}}_{d(k)|a(j)}} \right) e^{-\chi^{\text{net}}_{d(k)|a(j)}} \right] \right.$$

$$\times \left[\sum_{\bar{m}'=2}^{\infty} \frac{1}{\bar{m}'!} \left(\left(2\hat{\chi}^{\text{fan}}_{a(j)|d(k)} + 2\tilde{\chi}^{\text{fan}}_{a(j)|d(k)} \right)^{\bar{m}'} e^{-2\chi^{\text{net}}_{a(j)|d(k)}} - 2 \left(\tilde{\chi}^{\text{fan}}_{a(j)|d(k)} \right)^{\bar{m}'} e^{-\chi^{\text{net}}_{a(j)|d(k)}} \right) \right.$$

$$\left. + \left(1 - e^{-\chi^{\text{net}}_{a(j)|d(k)}} \right)^2 \right] + 2\chi^{\text{loop}_{\text{uu}}}_{a(j)|d(k)}(y_1, y', \vec{b}_1, \vec{b}'|Y, \vec{b})\, e^{-\chi^{\text{net}}_{a(j)|d(k)} - \chi^{\text{net}}_{d(k)|a(j)}} \sum_{\bar{m}'=2}^{\infty} \frac{\left(\tilde{\chi}^{\text{fan}}_{a(j)|d(k)} \right)^{\bar{m}'}}{\bar{m}'!} \right\}, \quad (62)$$

where the arguments of the eikonals in the integrand read $\chi^{\text{net}}_{a(j)|d(k)} = \chi^{\text{net}}_{a(j)|d(k)}(y', \vec{b}'|Y, \vec{b})$, $\hat{\chi}^{\text{fan}}_{a(j)|d(k)} = \hat{\chi}^{\text{fan}}_{a(j)|d(k)}(y', \vec{b}'|Y, \vec{b})$, $\tilde{\chi}^{\text{fan}}_{a(j)|d(k)} = \tilde{\chi}^{\text{fan}}_{a(j)|d(k)}(y', \vec{b}'|Y, \vec{b})$, $\chi^{\text{net}}_{d(k)|a(j)} = \chi^{\text{net}}_{d(k)|a(j)}(Y - y', \vec{b} - \vec{b}'|Y, \vec{b})$.

The contributions $2\bar{\chi}^{\text{loop}}_{a(j)|d(k)}$ and $2\tilde{\chi}^{\text{loop}}_{a(j)|d(k)}$ correspond to the subset of graphs obtained in case (i) above, being defined by the recursive equations (see Fig. 21)

$$\bar{\chi}^{\text{loop}}_{a(j)|d(k)}(y_1, \vec{b}_1|Y, \vec{b}) = \chi^{\text{loop}}_{a(j)}(y_1, b_1) + G \int_{\xi}^{y_1 - \xi} dy_2 \int d^2 b_2 \left(1 - e^{-\chi^{\text{loop}}(y_1 - y_2, |\vec{b}_1 - \vec{b}_2|)} \right)$$

$$\times \bar{\chi}^{\text{loop}}_{a(j)|d(k)}(y_2, \vec{b}_2|Y, \vec{b}) \left(e^{-2\chi^{\text{net}}_{a(j)|d(k)}(y_2, \vec{b}_2|Y, \vec{b}) - \chi^{\text{net}}_{d(k)|a(j)}(Y - y_2, \vec{b} - \vec{b}_2|Y, \vec{b})} - 1 \right) \quad (63)$$

27

Figure **21**: Recursive representations for the contributions $2\bar{\chi}^{\text{loop}}_{a(j)|d(k)} - 2\tilde{\chi}^{\text{loop}}_{a(j)|d(k)}$ (top) and $2\tilde{\chi}^{\text{loop}}_{a(j)|d(k)}$ (bottom) of the subsets of fanlike cuts of net-fans, which have a single cut Pomeron coupled to the projectile hadron.

$$\tilde{\chi}^{\text{loop}}_{a(j)|d(k)}(y_1,\vec{b}_1|Y,\vec{b}) = G \int_{\xi}^{y_1-\xi} dy_2 \int d^2 b_2 \left(1 - e^{-\chi^{\text{loop}}(y_1-y_2,|\vec{b}_1-\vec{b}_2|)}\right) \left[\bar{\chi}^{\text{loop}}_{a(j)|d(k)}(y_2,\vec{b}_2|Y,\vec{b})\right.$$

$$\times \left(1 - e^{-\chi^{\text{net}}_{d(k)|a(j)}(Y-y_2,\vec{b}-\vec{b}_2|Y,\vec{b})}\right) e^{-2\chi^{\text{net}}_{a(j)|d(k)}(y_2,\vec{b}_2|Y,\vec{b}) - \chi^{\text{net}}_{d(k)|a(j)}(Y-y_2,\vec{b}-\vec{b}_2|Y,\vec{b})}$$

$$\left. + \tilde{\chi}^{\text{loop}}_{a(j)|d(k)}(y_2,\vec{b}_2|Y,\vec{b}) \left(e^{-\chi^{\text{net}}_{a(j)|d(k)}(y_2,\vec{b}_2|Y,\vec{b}) - 2\chi^{\text{net}}_{d(k)|a(j)}(Y-y_2,\vec{b}-\vec{b}_2|Y,\vec{b})} - 1\right)\right]. \quad (64)$$

In a similar way, for the contributions $\chi^{\text{loop}_{xy}}_{a(j)|d(k)}(y_1,y',\vec{b}_1,\vec{b}'|Y,\vec{b})$ corresponding to t-channel sequences of multi-Pomeron vertices positioned between (y_1,b_1) and $(y',\vec{b}')$, coupled to uncut projectile and target net-fans and connected to each other and to the vertices (y_1,b_1), $(y',\vec{b}')$ by cut or uncut 2-point loop sequences [the index x (y) indicates whether the down-most (uppermost) loop sequence is cut, $x = $ c ($y = $ c), or uncut, $x = $ u ($y = $ u)], one obtains the equation system

$$\chi^{\text{loop}_{cc}}_{a(j)|d(k)}(y_1,y',\vec{b}_1,\vec{b}'|Y,\vec{b}) = \left[1 - e^{-\chi^{\text{loop}}(y_1-y',|\vec{b}_1-\vec{b}'|)}\right] + G \int_{y_1+\xi}^{y'-\xi} dy_2 \int d^2 b_2 \left[1 - e^{-\chi^{\text{loop}}(y_1-y_2,|\vec{b}_1-\vec{b}_2|)}\right]$$

$$\times \left[\chi^{\text{loop}_{cc}}_{a(j)|d(k)}(y_2,y',\vec{b}_2,\vec{b}'|Y,\vec{b}) \left(e^{-2\chi^{\text{net}}_{a(j)|d(k)} - 2\chi^{\text{net}}_{d(k)|a(j)}} - 1\right) - \chi^{\text{loop}_{uc}}_{a(j)|d(k)}(y_2,y',\vec{b}_2,\vec{b}'|Y,\vec{b})\right.$$

$$\left. \times \left(1 - e^{-\chi^{\text{net}}_{a(j)|d(k)}}\right) e^{-\chi^{\text{net}}_{a(j)|d(k)} - 2\chi^{\text{net}}_{d(k)|a(j)}}\right] \quad (65)$$

$$\chi^{\text{loop}_{cu}}_{a(j)|d(k)}(y_1,y',\vec{b}_1,\vec{b}'|Y,\vec{b}) = G \int_{y_1+\xi}^{y'-\xi} dy_2 \int d^2 b_2 \left[1 - e^{-\chi^{\text{loop}}(y_1-y_2,|\vec{b}_1-\vec{b}_2|)}\right]$$

$$\times \left[\chi^{\text{loop}_{cu}}_{a(j)|d(k)}(y_2,y',\vec{b}_2,\vec{b}'|Y,\vec{b}) \left(e^{-2\chi^{\text{net}}_{a(j)|d(k)} - 2\chi^{\text{net}}_{d(k)|a(j)}} - 1\right) + \chi^{\text{loop}_{uu}}_{a(j)|d(k)}(y_2,y',\vec{b}_2,\vec{b}'|Y,\vec{b})\right.$$

$$\left. \times \left(1 - e^{-\chi^{\text{net}}_{a(j)|d(k)}}\right) e^{-\chi^{\text{net}}_{a(j)|d(k)} - 2\chi^{\text{net}}_{d(k)|a(j)}}\right] \quad (66)$$

$$\chi^{\text{loop}_{uc}}_{a(j)|d(k)}(y_1,y',\vec{b}_1,\vec{b}'|Y,\vec{b}) = G \int_{y_1+\xi}^{y'-\xi} dy_2 \int d^2 b_2 \left[1 - e^{-\chi^{\text{loop}}(y_1-y_2,|\vec{b}_1-\vec{b}_2|)}\right]$$

$$\times \left[\chi^{\text{loop}_{cc}}_{a(j)|d(k)}(y_2,y',\vec{b}_2,\vec{b}'|Y,\vec{b}) \left(1 - e^{-\chi^{\text{net}}_{d(k)|a(j)}}\right) e^{-2\chi^{\text{net}}_{a(j)|d(k)} - \chi^{\text{net}}_{d(k)|a(j)}} + \chi^{\text{loop}_{uc}}_{a(j)|d(k)}(y_2,y',\vec{b}_2,\vec{b}'|Y,\vec{b})\right.$$

$$\left. \times \left(e^{-\chi^{\text{net}}_{a(j)|d(k)} - 2\chi^{\text{net}}_{d(k)|a(j)}} + e^{-2\chi^{\text{net}}_{a(j)|d(k)} - \chi^{\text{net}}_{d(k)|a(j)}} - e^{-2\chi^{\text{net}}_{a(j)|d(k)} - 2\chi^{\text{net}}_{d(k)|a(j)}} - 1\right)\right] \quad (67)$$

$$\chi_{a(j)|d(k)}^{\text{loop}_{\text{uu}}}(y_1, y', \vec{b}_1, \vec{b}'|Y, \vec{b}) = \left[1 - e^{-\chi^{\text{loop}}(y_1 - y', |\vec{b}_1 - \vec{b}'|)}\right] + G \int_{y_1+\xi}^{y'-\xi} dy_2 \int d^2 b_2 \left[1 - e^{-\chi^{\text{loop}}(y_1 - y_2, |\vec{b}_1 - \vec{b}_2|)}\right]$$

$$\times \left[-\chi_{a(j)|d(k)}^{\text{loop}_{\text{cu}}}(y_2, y', \vec{b}_2, \vec{b}'|Y, \vec{b}) \left(1 - e^{-\chi_{d(k)|a(j)}^{\text{net}}}\right) e^{-2\chi_{a(j)|d(k)}^{\text{net}} - \chi_{d(k)|a(j)}^{\text{net}}} + \chi_{a(j)|d(k)}^{\text{loop}_{\text{uu}}}(y_2, y', \vec{b}_2, \vec{b}'|Y, \vec{b})\right.$$

$$\left. \times \left(e^{-\chi_{a(j)|d(k)}^{\text{net}} - 2\chi_{d(k)|a(j)}^{\text{net}}} + e^{-2\chi_{a(j)|d(k)}^{\text{net}} - \chi_{d(k)|a(j)}^{\text{net}}} - e^{-2\chi_{a(j)|d(k)}^{\text{net}} - 2\chi_{d(k)|a(j)}^{\text{net}}} - 1\right)\right], \quad (68)$$

where the omitted arguments of the eikonals $\chi_{a(j)|d(k)}^{\text{net}}$, $\chi_{d(k)|a(j)}^{\text{net}}$ are the same as in Eqs. (63-64).

Appendix C

In case of nucleus-nucleus scattering, different cut and uncut Pomerons from the same irreducible graph may couple to different projectile and target nucleons. We start again from the contributions of fanlike cuts of net-fans, Fig. 5, for which we obtain

$$2\hat{\chi}_{A|B}^{\text{fan}}(y_1, \vec{b}_1|Y, \vec{b}) = \sum_{m=1}^{A} 2\chi_{p(j_m^A)}^{\text{loop}}(y_1, |\vec{b}_1 - \vec{b}_m^A|) + G \int_{\xi}^{y_1-\xi} dy_2 \int d^2 b_2 \left(1 - e^{-\chi^{\text{loop}}(y_1 - y_2, |\vec{b}_1 - \vec{b}_2|)}\right)$$

$$\times \left\{\left[\left(e^{2\tilde{\chi}_{A|B}^{\text{fan}}(y_2, \vec{b}_2|Y, \vec{b})} - 1\right) e^{-2\chi_{A|B}^{\text{net}}(y_2, \vec{b}_2|Y, \vec{b}) - 2\chi_{B|A}^{\text{net}}(Y - y_2, \vec{b} - \vec{b}_2|Y, \vec{b})} - 2\tilde{\chi}_{A|B}^{\text{fan}}(y_2, \vec{b}_2|Y, \vec{b})\right]\right.$$

$$-2\left[\left(e^{\tilde{\chi}_{A|B}^{\text{fan}}(y_2, \vec{b}_2|Y, \vec{b})} - 1\right) e^{-\chi_{A|B}^{\text{net}}(y_2, \vec{b}_2|Y, \vec{b}) - 2\chi_{B|A}^{\text{net}}(Y - y_2, \vec{b} - \vec{b}_2|Y, \vec{b})} - \tilde{\chi}_{A|B}^{\text{fan}}(y_2, \vec{b}_2|Y, \vec{b})\right]$$

$$\left. + \left(1 - e^{-\chi_{A|B}^{\text{net}}(y_2, \vec{b}_2|Y, \vec{b})}\right)^2 e^{-2\chi_{B|A}^{\text{net}}(Y - y_2, \vec{b} - \vec{b}_2|Y, \vec{b})}\right\} \quad (69)$$

$$2\tilde{\chi}_{A|B}^{\text{fan}}(y_1, \vec{b}_1|Y, \vec{b}) = G \int_{\xi}^{y_1-\xi} dy_2 \int d^2 b_2 \left(1 - e^{-\chi^{\text{loop}}(y_1 - y_2, |\vec{b}_1 - \vec{b}_2|)}\right)$$

$$\times \left\{\left(1 - e^{-\chi_{B|A}^{\text{net}}(Y - y_2, \vec{b} - \vec{b}_2|Y, \vec{b})}\right) e^{-\chi_{B|A}^{\text{net}}(Y - y_2, \vec{b} - \vec{b}_2|Y, \vec{b})} \left[\left(e^{2\tilde{\chi}_{A|B}^{\text{fan}}(y_2, \vec{b}_2|Y, \vec{b})} - 1\right) e^{-2\chi_{A|B}^{\text{net}}(y_2, \vec{b}_2|Y, \vec{b})}\right.\right.$$

$$\left. - 2\left(e^{\tilde{\chi}_{A|B}^{\text{fan}}(y_2, \vec{b}_2|Y, \vec{b})} - 1\right) e^{-\chi_{A|B}^{\text{net}}(y_2, \vec{b}_2|Y, \vec{b})} + \left(1 - e^{-\chi_{A|B}^{\text{net}}(y_2, \vec{b}_2|Y, \vec{b})}\right)^2\right]$$

$$\left. + 2\left[\left(e^{\tilde{\chi}_{A|B}^{\text{fan}}(y_2, \vec{b}_2|Y, \vec{b})} - 1\right) e^{-\chi_{A|B}^{\text{net}}(y_2, \vec{b}_2|Y, \vec{b}) - \chi_{B|A}^{\text{net}}(Y - y_2, \vec{b} - \vec{b}_2|Y, \vec{b})} - \tilde{\chi}_{A|B}^{\text{fan}}(y_2, \vec{b}_2|Y, \vec{b})\right]\right\}, \quad (70)$$

where $2\hat{\chi}_{A|B}^{\text{fan}}$ corresponds to cut graphs where the handle of the fan is cut, $2\tilde{\chi}_{A|B}^{\text{fan}}$ - to the ones where it is uncut, and $2\bar{\chi}_{A|B}^{\text{fan}} = 2\hat{\chi}_{A|B}^{\text{fan}} + 2\tilde{\chi}_{A|B}^{\text{fan}}$ is the total contribution of fanlike cuts of net-fans; the dependence of the eikonals on the coordinates and eigenstates of all the nucleons is not shown explicitly.

We are going to proceed like in Appendix A, expanding $\bar{\chi}_{A|B}^{\text{fan}}$, $\hat{\chi}_{A|B}^{\text{fan}}$, and $\tilde{\chi}_{A|B}^{\text{fan}}$ as

$$\bar{\chi}_{A|B}^{\text{fan}}(y_1, \vec{b}_1|Y, \vec{b}) = \sum_{m=1}^{A} \bar{\chi}_{p(j_m^A)}^{\text{fan}}(y_1, |\vec{b}_1 - \vec{b}_m^A|, \ldots) \quad (71)$$

$$\hat{\chi}_{A|B}^{\text{fan}}(y_1, \vec{b}_1|Y, \vec{b}) = \sum_{m=1}^{A} \hat{\chi}_{p(j_m^A)}^{\text{fan}}(y_1, |\vec{b}_1 - \vec{b}_m^A|, \ldots), \quad (72)$$

$$\tilde{\chi}_{p(j_m^A)}^{\text{fan}}(y_1, |\vec{b}_1 - \vec{b}_m^A|, \ldots) = \bar{\chi}_{p(j_m^A)}^{\text{fan}}(y_1, |\vec{b}_1 - \vec{b}_m^A|, \ldots) - \hat{\chi}_{p(j_m^A)}^{\text{fan}}(y_1, |\vec{b}_1 - \vec{b}_m^A|, \ldots) \quad (73)$$

and approximating the dependence on the coordinates and eigenstates of all the $A+B-1$ projectile and target nucleons but the current one by some factors.

Adding (69) to (70), substituting the decompositions (47), (71-73), and using the identities

$$\exp\left(2\sum_{m=1}^{A} \bar{\chi}_{p(j_m^A)}^{\text{fan}}\right) - 1 = \sum_{m=1}^{A} \left(e^{2\bar{\chi}_{p(j_m^A)}^{\text{fan}}} - 1\right) e^{2\sum_{l=m+1}^{A} \bar{\chi}_{p(j_l^A)}^{\text{fan}}} \quad (74)$$

$$\exp\left(\sum_{m=1}^{A}\tilde{\chi}^{\text{fan}}_{p(j_m^A)}\right)-1=\sum_{m=1}^{A}\left(e^{\tilde{\chi}^{\text{fan}}_{p(j_m^A)}}-1\right)e^{\sum_{l=m+1}^{A}\tilde{\chi}^{\text{fan}}_{p(j_l^A)}}\tag{75}$$

$$\left[1-\exp\left(-\sum_{m=1}^{A}\chi^{\text{net}}_{p(j_m^A)}\right)\right]^2=\sum_{m=1}^{A}\left[\left(1-e^{-\chi^{\text{net}}_{p(j_m^A)}}\right)^2e^{-2\sum_{l=1}^{m-1}\chi^{\text{net}}_{p(j_l^A)}}\right.$$
$$\left.+2\left(1-e^{-\chi^{\text{net}}_{p(j_m^A)}}\right)\left(1-e^{-\sum_{l=1}^{m-1}\chi^{\text{net}}_{p(j_l^A)}}\right)e^{-\sum_{l=1}^{m-1}\chi^{\text{net}}_{p(j_l^A)}}\right],\tag{76}$$

we obtain

$$\sum_{m=1}^{A}2\bar{\chi}^{\text{fan}}_{p(j_m^A)}(y_1,|\vec{b}_1-\vec{b}_m^A|,\ldots)=\sum_{m=1}^{A}\left\{2\chi^{\text{loop}}_{p(j_m^A)}(y_1,|\vec{b}_1-\vec{b}_m^A|)+G\int_\xi^{y_1-\xi}dy_2\int d^2b_2\right.$$
$$\times\left(1-e^{-\chi^{\text{loop}}}\right)\left[\left(e^{2(\bar{\chi}^{\text{fan}}_{p(j_m^A)}-\chi^{\text{net}}_{p(j_m^A)})}-e^{-2\chi^{\text{net}}_{p(j_m^A)}}\right)e^{2\sum_{l=m+1}^{A}(\bar{\chi}^{\text{fan}}_{p(j_l^A)}-\chi^{\text{net}}_{p(j_l^A)})}\left(Z^{(m)}_{A|B}\right)^2\right.$$
$$\left.\left.-2\bar{\chi}^{\text{fan}}_{p(j_m^A)}+\left(1-e^{-\chi^{\text{net}}_{p(j_m^A)}}\right)^2\left(Z^{(m)}_{A|B}\right)^2+2\left(1-e^{-\chi^{\text{net}}_{p(j_m^A)}}\right)Z^{(m)}_{A|B}\left(1-Z^{(m)}_{A|B}\right)\right]\right\},\tag{77}$$

where the arguments of the eikonals in the integrand are the same as in (49) and $Z^{(m)}_{A|B}$ is defined in (50).

Comparing (77) to (49), we obtain

$$\bar{\chi}^{\text{fan}}_{p(j_m^A)}(y_1,|\vec{b}_1-\vec{b}_m^A|,\ldots)=\chi^{\text{net}}_{p(j_m^A)}(y_1,|\vec{b}_1-\vec{b}_m^A|,\ldots).\tag{78}$$

Now, substituting (47), (71-73) into (69), using (74-76), (78), and doing the same approximation as in (51), we obtain

$$\hat{\chi}^{\text{fan}}_{A|B}(y_1,\vec{b}_1|Y,\vec{b})=\sum_{m=1}^{A}\hat{\chi}^{\text{fan}}_{p(j_m^A)}\Big(y_1,|\vec{b}_1-\vec{b}_m^A|,Z^{(m)}_{A|B}(y_1,\vec{b}_1,Y,\vec{b},\{j^A,k^B,\vec{b}^A,\vec{b}^B\}),$$
$$\hat{Z}^{(m)}_A(y_1,\vec{b}_1,Y,\vec{b},\{j^A,k^B,\vec{b}^A,\vec{b}^B\}),Z_B(Y-y_1,\vec{b}-\vec{b}_1,Y,\vec{b},\{k^B,j^A,\vec{b}^B,\vec{b}^A\})\Big),\tag{79}$$

where we introduced

$$\hat{Z}^{(m)}_A(y_1,\vec{b}_1,Y,\vec{b},\{j^A,k^B,\vec{b}^A,\vec{b}^B\})=\exp\left[-\sum_{l=m+1}^{A}\hat{\chi}^{\text{fan}}_{p(j_l^A)}(y_1,|\vec{b}_1-\vec{b}_l^A|,Z^{(l)}_{A|B},\hat{Z}^{(l)}_A,Z_B)\right]\tag{80}$$

$$Z_A(y_1,\vec{b}_1,Y,\vec{b},\{j^A,k^B,\vec{b}^A,\vec{b}^B\})=\exp\left[-\sum_{l=1}^{A}\chi^{\text{net}}_{p(j_l^A)}(y_1,|\vec{b}_1-\vec{b}_l^A|,Z^{(m)}_{A|B})\right]\tag{81}$$

and $\hat{\chi}^{\text{fan}}_{p(j_m^A)}$ is defined by the equation

$$\hat{\chi}^{\text{fan}}_{p(j)}(y_1,b',Z_1,Z_2,Z_3)=\chi^{\text{loop}}_{p(j)}(y_1,b')+G\int_\xi^{y_1-\xi}dy_2\int d^2b_2\left(1-e^{-\chi^{\text{loop}}(y_1-y_2,|\vec{b}'-\vec{b}_2|)}\right)$$
$$\times\left[\left(1-e^{-\hat{\chi}^{\text{fan}}_{p(j)}(y_2,b_2,Z_1,Z_2,Z_3)}\right)Z_1Z_2Z_3-\hat{\chi}^{\text{fan}}_{p(j)}(y_2,b_2,Z_1,Z_2,Z_3)\right.$$
$$\left.+\left(1-e^{-\chi^{\text{net}}_{p(j)}(y_2,b_2,Z_1)}\right)Z_1Z_3(1-Z_2)\right].\tag{82}$$

In a similar way we can obtain contributions of other subsets of cut net-fan graphs, defined in Appendix B, and apply them to decompose partial opacities for various macro-configurations of

nucleus-nucleus collisions (as defined in Fig. 6) in the form resembling binarylike nucleon-nucleon collisions [cf. (54-55)]:

$$\bar{\Omega}_{AB}^{(i)}(s,b,\{j^A,k^B,\vec{b}^A,\vec{b}^B\}) = \sum_{m=1}^{A}\sum_{n=1}^{B}\bar{\Omega}_{mn}^{(i)}(s,b,\{j^A,k^B,\vec{b}^A,\vec{b}^B\})\,, \tag{83}$$

which satisfy

$$\sum_{i=1}^{11}\bar{\Omega}_{mn}^{(i)}(s,b,\{j^A,k^B,\vec{b}^A,\vec{b}^B\}) = \Omega_{AB}^{(mn)}(s,b,\{j^A,k^B,\vec{b}^A,\vec{b}^B\})\,, \tag{84}$$

with $\Omega_{AB}^{(mn)}$ being defined in (57). Such a decomposition is a useful technical trick for the MC implementation of the approach: Each term in the decomposition corresponds to an inelastic rescattering process between a given pair (mn) of the projectile and target nucleons but generally involves additional inelastic rescatterings on other nucleons of the two nuclei.

For example, for the configuration defined by the graphs in the 1st square bracket in Fig. 6 one obtains

$$\bar{\Omega}_{mn}^{(1)} = \frac{G}{2}\int_{\xi}^{Y-\xi}dy_1\int d^2b_1\left\{\left[\left(1-e^{-2\chi_{p(j_m^A)}^{\rm net}}\right)e^{-2\sum_{l=1}^{m-1}\chi_{p(j_l^A)}^{\rm net}}-2\chi_{p(j_m^A)}^{\rm net}\,e^{-2\sum_{l=1}^{A}\chi_{p(j_l^A)}^{\rm net}}\right]\right.$$

$$\times\left[\left(1-e^{-2\chi_{p(k_n^B)}^{\rm net}}\right)e^{-2\sum_{i=1}^{n-1}\chi_{p(k_i^B)}^{\rm net}}-2\chi_{p(k_n^B)}^{\rm net}\,e^{-2\sum_{i=1}^{B}\chi_{p(k_i^B)}^{\rm net}}\right]$$

$$-2\left[\left(1-e^{-2\chi_{p(j_m^A)}^{\rm net}}\right)e^{-2\sum_{l=1}^{m-1}\chi_{p(j_l^A)}^{\rm net}}-2\chi_{p(j_m^A)}^{\rm net}\,e^{-2\sum_{l=1}^{A}\chi_{p(j_l^A)}^{\rm net}}\right]$$

$$\times\left[\left(e^{\tilde{\chi}_{p(k_n^B)}^{\rm fan}}-1\right)e^{\sum_{i=n+1}^{B}\tilde{\chi}_{p(k_i^B)}^{\rm fan}}-\tilde{\chi}_{p(k_n^B)}^{\rm fan}\right]e^{-\sum_{i=1}^{B}\chi_{p(k_i^B)}^{\rm net}}$$

$$-2\left[\left(e^{\tilde{\chi}_{p(j_m^A)}^{\rm fan}}-1\right)e^{\sum_{l=m+1}^{A}\tilde{\chi}_{p(j_l^A)}^{\rm fan}}-\tilde{\chi}_{p(j_m^A)}^{\rm fan}\right]e^{-\sum_{l=1}^{A}\chi_{p(j_l^A)}^{\rm net}}$$

$$\times\left.\left[\left(1-e^{-2\chi_{p(k_n^B)}^{\rm net}}\right)e^{-2\sum_{i=1}^{n-1}\chi_{p(k_i^B)}^{\rm net}}-2\chi_{p(k_n^B)}^{\rm net}\,e^{-2\sum_{i=1}^{B}\chi_{p(k_i^B)}^{\rm net}}\right]\right\}. \tag{85}$$

Using (84), we can easily write down the absorptive nucleus-nucleus cross section:

$$\sigma_{AB}^{\rm abs}(s) = \int d^2b\left\langle\left\langle\prod_{m=1}^{A}\prod_{n=1}^{B}\left[\sum_{N_{mn}=0}^{\infty}\frac{\left[\sum_{i=1}^{11}\bar{\Omega}_{mn}^{(i)}\right]^{N_{mn}}}{N_{mn}!}e^{-\Omega_{AB}^{(mn)}(s,b,\{j^A,k^B,\vec{b}^A,\vec{b}^B\})}\right]\right.\right.$$

$$-\left.\left.\prod_{m=1}^{A}\prod_{n=1}^{B}e^{-\Omega_{AB}^{(mn)}(s,b,\{j^A,k^B,\vec{b}^A,\vec{b}^B\})}\right\rangle_A\right\rangle_B = \int d^2b\left\langle\left\langle1-e^{-\sum_{m=1}^{A}\sum_{n=1}^{B}\Omega_{AB}^{(mn)}(s,b,\{j^A,k^B,\vec{b}^A,\vec{b}^B\})}\right\rangle_A\right\rangle_B, \tag{86}$$

which can be applied for a MC treatment of inelastic nucleus-nucleus (hadron-nucleus) collisions. It is worth stressing again that partial opacities $\bar{\Omega}_{mn}^{(i)}$ generally correspond not only to an inelastic rescattering between m-th projectile and n-th target nucleons but involve also inelastic interactions with $(m+1)$-th, $\cdots$, A-th projectile and $(n+1)$-th, $\cdots$, B-th target nucleons.

Appendix D

The relations of Appendix B allow one to reconstruct the cut Pomeron structure for a cut net-fan contribution. For simplicity, we shall illustrate the procedure neglecting the production of large rapidity gaps at central rapidities, i.e. neglecting the contributions of Pomeron loops and the ones
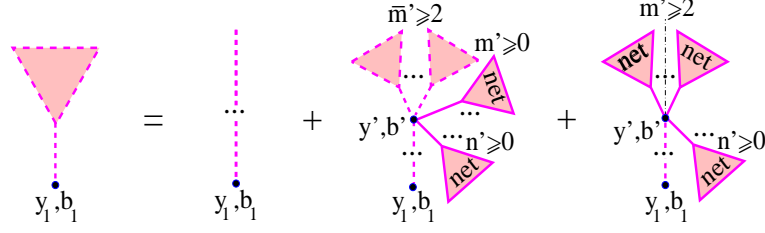
Figure **22**: Recursive representation for the contribution of fanlike cuts of net-fans, Pomeron loops and central rapidity gaps neglected.

of fanlike cuts of net-fans, which leave the handle of the fan uncut. Thus, we use $2\bar{\chi}^{\text{fan}}_{a(j)|d(k)} = 2\hat{\chi}^{\text{fan}}_{a(j)|d(k)}$, $2\tilde{\chi}^{\text{fan}}_{a(j)|d(k)} = 0$ and the representation of Fig. 19 takes the form (see Fig. 22)

$$2\bar{\chi}^{\text{fan}}_{a(j)|d(k)}(y_1,\vec{b}_1|Y,\vec{b}) = 2\bar{\chi}^{\mathbb{P}}_{a(j)|d(k)}(y_1,\vec{b}_1|Y,\vec{b}) + G\int_\xi^{y_1-\xi}dy'\int d^2b'\,\chi^{\mathbb{P}_{\text{cc}}}_{a(j)|d(k)}(y_1,y',\vec{b}_1,\vec{b}'|Y,\vec{b})$$

$$\times e^{-2\chi^{\text{net}}_{d(k)|a(j)}}\left[\sum_{\bar{m}'=2}^\infty\frac{\left(2\bar{\chi}^{\text{fan}}_{a(j)|d(k)}\right)^{\bar{m}'}}{\bar{m}'!}e^{-2\chi^{\text{net}}_{a(j)|d(k)}} + \left(1-e^{-\chi^{\text{net}}_{a(j)|d(k)}}\right)^2\right],\quad(87)$$

where the omitted arguments of the eikonals in the integrand are the same as in (61) and the 1st term in the r.h.s., $2\bar{\chi}^{\mathbb{P}}_{a(j)|d(k)}(y_1,\vec{b}_1|Y,\vec{b})$, is the contribution of a t-channel sequence of cut Pomerons, exchanged between the vertex $(y_1,\vec{b}_1)$ and the projectile hadron, with the multi-Pomeron vertices which couple neighboring Pomerons to each other being connected to at least one uncut projectile or target net-fan. Similarly, $2\chi^{\mathbb{P}_{\text{cc}}}_{a(j)|d(k)}(y_1,y',\vec{b}_1,\vec{b}'|Y,\vec{b})$ defines the contribution of such a cut Pomeron sequence exchanged between the vertices $(y_1,\vec{b}_1)$ and $(y',\vec{b}')$. The two contributions are defined by recursive equations [cf. (63), (65)]

$$\bar{\chi}^{\mathbb{P}}_{a(j)|d(k)}(y_1,\vec{b}_1|Y,\vec{b}) = \chi^{\mathbb{P}}_{a(j)}(y_1,b_1) + G\int_\xi^{y_1-\xi}dy_2\int d^2b_2\,\chi^{\mathbb{P}}(y_1-y_2,|\vec{b}_1-\vec{b}_2|)$$

$$\times\bar{\chi}^{\mathbb{P}}_{a(j)|d(k)}(y_2,\vec{b}_2|Y,\vec{b})\left[e^{-2\chi^{\text{net}}_{a(j)|d(k)}(y_2,\vec{b}_2|Y,\vec{b})-2\chi^{\text{net}}_{d(k)|a(j)}(Y-y_2,\vec{b}-\vec{b}_2|Y,\vec{b})}-1\right]\quad(88)$$

$$\chi^{\mathbb{P}_{\text{cc}}}_{a(j)|d(k)}(y_1,y',\vec{b}_1,\vec{b}'|Y,\vec{b}) = \chi^{\mathbb{P}}(y_1-y',|\vec{b}_1-\vec{b}'|) + G\int_{y_1+\xi}^{y'-\xi}dy_2\int d^2b_2\,\chi^{\mathbb{P}}(y_1-y_2,|\vec{b}_1-\vec{b}_2|)$$

$$\times\chi^{\mathbb{P}_{\text{cc}}}_{a(j)|d(k)}(y_2,y',\vec{b}_2,\vec{b}'|Y,\vec{b})\left[e^{-2\chi^{\text{net}}_{a(j)|d(k)}(y_2,\vec{b}_2|Y,\vec{b})-2\chi^{\text{net}}_{d(k)|a(j)}(Y-y_2,\vec{b}-\vec{b}_2|Y,\vec{b})}-1\right].\quad(89)$$

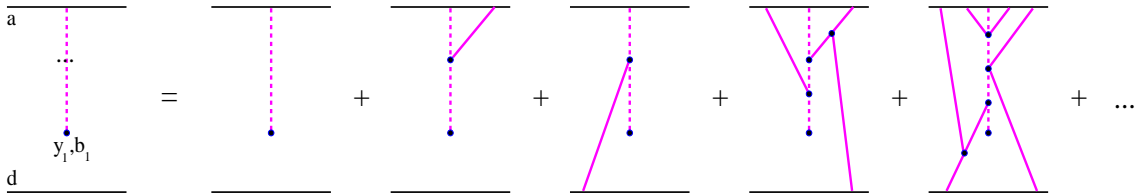Examples of diagrams generated by Eq. (88) are depicted in Fig. 23. The corresponding piece

Figure **23**: Examples of cut diagrams corresponding to a single t-channel sequence of cut Pomerons exchanged between the vertex $(y_1,\vec{b}_1)$ and the projectile hadron.

of secondary hadron production is represented by a single chain of particles produced between

the projectile hadron and the vertex $(y_1, \vec{b}_1)$, as defined by the 1st graph in the r.h.s. of the figure (single cut Pomeron exchange). All the other graphs in the r.h.s. have the same particle production pattern and describe absorptive corrections to the process due to virtual (elastic) rescatterings on the projectile and target hadrons of intermediate partons of the underlying parton cascade.

Using Eq. (87), one can easily generate the cut structure for the contribution $2\bar{\chi}^{\text{fan}}_{a(j)|d(k)}(y_1, \vec{b}_1|Y, \vec{b})$. With the probability $w_{1\mathbb{P}} = \bar{\chi}^{\mathbb{P}}_{a(j)|d(k)}(y_1, \vec{b}_1|Y, \vec{b})/\bar{\chi}^{\text{fan}}_{a(j)|d(k)}(y_1, \vec{b}_1|Y, \vec{b})$, the particle production pattern is the one of a single cut Pomeron exchange between the projectile hadron and the vertex $(y_1, \vec{b}_1)$. In the opposite case, sampled with the probability $1 - w_{1\mathbb{P}}$, one generates the rapidity y' and transverse vector $\vec{b}'$ of the new multi-Pomeron vertex - according to the integrand of the 2nd term in the r.h.s. of Eq. (87). Then, with the partial probability

$$w_{\text{gap}} = \frac{\left(1 - e^{-\chi^{\text{net}}_{a(j)|d(k)}}\right)^2}{\left(1 - e^{-\chi^{\text{net}}_{a(j)|d(k)}}\right)^2 + \left(e^{2\bar{\chi}^{\text{fan}}_{a(j)|d(k)}} - 1 - 2\bar{\chi}^{\text{fan}}_{a(j)|d(k)}\right)e^{-2\chi^{\text{net}}_{a(j)|d(k)}}}$$

the corresponding piece of the final state consists of a single chain of secondaries produced in the rapidity interval $[y_1, y']$ [single cut Pomeron exchange between $(y_1, \vec{b}_1)$ and $(y', \vec{b}')$], with the projectile hadron being separated from the particles produced by a LRG. Alternatively, with the probability $1 - w_{\text{gap}}$, one obtains a fanlike structure for the particle production pattern: In addition to the above-mentioned chain of secondaries, produced in the interval $[y_1, y']$, secondary particles emerge from $\bar{m}' \geq 2$ cut net-fans exchanged between the vertex $(y', \vec{b}')$ and the projectile hadron. In such a case, one generates the number of cut net-fans $\bar{m}'$ according to the Poisson distribution with the mean $2\bar{\chi}^{\text{fan}}_{a(j)|d(k)}$ (rejecting the cases $\bar{m}' \leq 1$) and applies the above-discussed procedure recursively for each of the $\bar{m}'$ cut net-fans.

Taking into consideration Pomeron loops and central rapidity gaps, the procedure remains qualitatively similar, being then based on Eqs. (61-68). The difference compared to the above-discussed treatment is that instead of t-channel sequences of cut Pomerons (as exemplified in Fig. 23) one generally obtains cut t-channel sequences of Pomerons and Pomeron loops, which are connected to each other by multi-Pomeron vertices coupled to uncut net-fans. Hence, a similar algorithm is applied to reconstruct the cut Pomeron structure of those cut loop sequences.

Appendix E

To illustrate the effect of zigzaglike cut contributions, let us consider the simplest cut graphs of that kind shown in Fig. 24 (a,b). The contribution of the graph in Fig. 24 (a) is
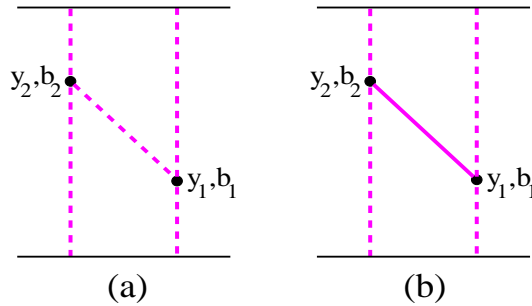

Figure **24**: Lowest order zigzaglike cut diagrams.

$$\Delta\hat{\Omega}^{\text{zz}}_{ad(jk)}(s, b) = 8G^2 \int d^2b_1 d^2b_2 \int_{\xi}^{Y-2\xi} dy_1 \int_{y_1+\xi}^{Y-\xi} dy_2 \, \chi^{\mathbb{P}}_{a(j)}(Y - y_1, |\vec{b} - \vec{b}_1|)$$

$$\times \chi_{a(j)}^{\mathbb{P}}(Y - y_2, |\vec{b} - \vec{b}_2|) \, \chi_{d(k)}^{\mathbb{P}}(y_1, b_1) \, \chi_{d(k)}^{\mathbb{P}}(y_2, b_2) \, \chi^{\mathbb{P}}(y_2 - y_1, |\vec{b}_2 - \vec{b}_1|) \,, \tag{90}$$

and the one of the graph in Fig. 24 (b) is defined by the same expression up to a sign, $\Delta\tilde{\Omega}_{ad(jk)}^{\mathrm{zz}}(s,b) = -\Delta\hat{\Omega}_{ad(jk)}^{\mathrm{zz}}(s,b)$. The diagram in Fig. 24 (b) provides a (negative) screening correction to the eikonal configuration with two cut Pomerons. On the other hand, the one in Fig. 24 (a) introduces a new process, with the weight being equal to the one of the mentioned screening contribution, and with the particle production pattern being almost identical to the one of Fig. 24 (b); the only difference arises from the cut Pomeron exchanged between the vertices (y_1, b_1) and (y_2, b_2). Thus, the combined effect of these two graphs is to provide additional particle production in the rapidity interval $[y_1, y_2]$. Hence, to account for the contributions of the graphs of Fig. 24 to secondary particle production, one has to select final state configurations with just two cut Pomerons exchanged and, with the probability $w_{\mathrm{zz}} = \Delta\hat{\Omega}_{ad(jk)}^{\mathrm{zz}}(s,b)/(\Omega_{ad(jk)}^{(2\mathbb{P})}(s,b)$ [$\Omega_{ad(jk)}^{(2\mathbb{P})}(s,b)$ being the partial weight of the two cut Pomerons process] to add an additional cut Pomeron exchange between the vertices (y_1, b_1) and (y_2, b_2), with the rapidity and transverse coordinates of the vertices being generated according to the integrand of Eq. (90). At sufficiently high energies $\Delta\hat{\Omega}_{ad(jk)}^{\mathrm{zz}}(s,b) > \Omega_{ad(jk)}^{(2\mathbb{P})}(s,b)$ due to the faster energy rise of the enhanced graph contributions. A simple effective procedure would then be to consider w_{zz} as the mean number of additional Pomerons to be added to the initial configuration.

The general treatment of zigzaglike cut graphs follows the above-discussed logic. We restrict ourselves with the set of zigzaglike cut graphs which provide nonzero contribution to *inclusive* particle spectra and split it into two subsets whose contributions are equal up to a sign: $\hat{\Omega}_{ad(jk)}^{\mathrm{zz}}(s,b) = -\tilde{\Omega}_{ad(jk)}^{\mathrm{zz}}(s,b)$, where $\hat{\Omega}_{ad(jk)}^{\mathrm{zz}}$ can be written as

$$\hat{\Omega}_{ad(jk)}^{\mathrm{zz}}(s,b) = \int d^2 b_1 d^2 b_2 \int_{\xi}^{Y-2\xi} dy_1 \int_{y_1+\xi}^{Y-\xi} dy_2 \, 2\chi_{ad|jk}^{\mathrm{zz}}(y_1, y_2, \vec{b}_1, \vec{b}_2 | Y, \vec{b}) \,. \tag{91}$$

The particle production pattern is almost identical for the contributions $\hat{\Omega}_{ad(jk)}^{\mathrm{zz}}$ and $\tilde{\Omega}_{ad(jk)}^{\mathrm{zz}}$, except that the former contains a *cut* sequence of Pomerons and Pomeron loops exchanged between the vertices (y_1, b_1) and (y_2, b_2) (with internal multi-Pomeron vertices in the sequence being generally coupled to *uncut* projectile and/or target net-fans) while the same sequence remains *uncut* in the latter contribution. Thus, the combined effect of both subsets of graphs is to add additional cut Pomerons resulting from this cut loop sequence. For brevity, we shall not discuss the corresponding technical implementation.

References

[1] P. Aurenche *et al.*, Phys. Rev. D **45**, 92 (1992).

[2] K. Werner, F.-M. Liu and T. Pierog, Phys. Rev. C **74**, 044902 (2006).

[3] N. N. Kalmykov, S. S. Ostapchenko and A. I. Pavlov, Nucl. Phys. Proc. Suppl. **52B**, 17 (1997); INP MSU 98-36/537, Moscow 1998.

[4] E.-J. Ahn *et al.*, Phys. Rev. D **80**, 094003 (2009).

[5] V. N. Gribov, Sov. Phys. JETP **26**, 414 (1968); *ibid.* **29**, 483 (1969).

[6] N.N. Kalmykov, S.S. Ostapchenko, and A.I. Pavlov, Bull. Russ. Acad. Sci. Phys. **58**, 1966 (1994).

[7] H.J. Drescher *et al.*, J. Phys. G **25**, L91 (1999); S. Ostapchenko *et al.*, *ibid.* **28**, 2597 (2002).

[8] L. Gribov, E. Levin, and M. Ryskin, Phys. Rep. **100**, 1 (1983); A. H. Mueller and J. w. Qui, Nucl. Phys. B **268**, 427 (1986).

[9] O. V. Kancheli, JETP Lett. **18**, 274 (1973); A. Schwimmer, Nucl. Phys. B **94**, 445 (1975); A. Capella, J. Kaplan and J. Tran Thanh Van, *ibid.* **105**, 333 (1976); V. A. Abramovskii, JETP Lett. **23**, 228 (1976); M. S. Dubovikov and K. A. Ter-Martirosyan, Nucl. Phys. B **124**, 163 (1977).

[10] J. L. Cardi, Nucl. Phys. B **75**, 413 (1974).

[11] A. B. Kaidalov, L. A. Ponomarev and K. A. Ter-Martirosyan, Sov. J. Nucl. Phys. **44**, 468 (1986).

[12] S. Ostapchenko, Phys. Lett. B **636**, 40 (2006).

[13] S. Ostapchenko, Phys. Rev. D **77**, 034009 (2008).

[14] S. Ostapchenko, Phys. Rev. D **81**, 114028 (2010).

[15] S. Ostapchenko, in preparation.

[16] M. L. Good and W. D. Walker, Phys. Rev. **120**, 1857 (1960).

[17] A. B. Kaidalov, Phys. Rep. **50**, 157 (1979).

[18] A. B. Kaidalov and K. A. Ter-Martirosyan, Phys. Lett. B **117**, 247 (1982).

[19] H. J. Drescher *et al.*, Phys. Rep. **350**, 93 (2001).

[20] S. Ostapchenko, Phys. Rev. D **74**, 014026 (2006).

[21] N. N. Kalmykov and S. S. Ostapchenko, Phys. Atom. Nucl. **56**, 346 (1993).

[22] V. A. Abramovsky, V. N. Gribov and O. V. Kancheli, Sov. J. Nucl. Phys. **18**, 308 (1974).

[23] K. Werner, Phys. Rev. D **39**, 780 (1989).

[24] A. B. Kaidalov, Sov. J. Nucl. Phys. **45**, 902 (1987).

[25] K. Nakamura *et al.* (Particle Data Group), J. Phys. G **37**, 075021 (2010).

[26] A. Breakstone *et al.*, Nucl. Phys. B **248**, 253 (1984).

[27] R. Battiston *et al.* (UA1 Collaboration), Phys. Lett. **127B**, 472 (1983).

[28] M. Bozzo *et al.* (UA4 Collaboration), Phys. Lett. **147B**, 385 (1985); *ibid.* **155B**, 197 (1985).

[29] N. A. Amos *et al.* (E710 Collaboration), Phys. Lett. B **247**, 127 (1990).

[30] F. Abe *et al.* (CDF Collaboration), Phys. Rev. D **50**, 5518 (1994).

[31] M. Adamus *et al.*, Phys. Lett. B **186**, 223 (1987).

[32] F. D. Aaron *et al.* (H1 and ZEUS Collaboration), JHEP **1001**, 109 (2010).

[33] S. Chekanov *et al.* (ZEUS Collaboration), Nucl. Phys. B **816**, 1 (2009).

[34] A. Aktas *et al.* (H1 Collaboration), Eur. Phys. J. C **48**, 749 (2006).

[35] N. N. Nikolaev and B. G. Zakharov, Z. Phys. C **53**, 331 (1992); M. Genovese, N. N. Nikolaev and B. G. Zakharov, J. Exp. Theor. Phys. **81**, 625 (1995); J. Bartels, J. R. Ellis, H. Kowalski and M. Wusthoff, Eur. Phys. J. C **7**, 443 (1999).

[36] F. Abe *et al.* (CDF Collaboration), Phys. Rev. D **50**, 5535 (1994).

[37] T. Affolder *et al.* (CDF Collaboration), Phys. Rev. Lett. **87**, 141802 (2001).

[38] A. E. Brenner *et al.*, Phys. Rev. D **26**, 1497 (1982).

[39] J. Whitmore, Phys. Rep. **10**, 273 (1974).

[40] C. Alt *et al.* (NA49 Collaboration), Eur. Phys. J. C **45**, 343 (2006).

[41] G. J. Alner *et al.* (UA5 Collaboration), Z. Phys. C **33**, 1 (1986).

[42] C. Albajar *et al.* (UA1 Collaboration), Nucl. Phys. B **335**, 261 (1990).

[43] F. Abe *et al.* (CDF Collaboration), Phys. Rev. D **41**, 2330 (1990).

[44] F. Abe *et al.* (CDF Collaboration), Phys. Rev. Lett. **61** (1988) 1819.

[45] V. Khachatryan *et al.* (CMS Collab.), Phys. Rev. Lett. **105** (2010) 022002.

[46] V. A. Khoze, A. D. Martin and M. G. Ryskin, Phys. Lett. B **679**, 56 (2009).

[47] V. Berardi *et al.* (TOTEM Collaboration), CERN-LHCC-2004-002, Jan 2004; CERN-LHCC-2004-020, Jun 2004.

[48] G. Aad *et al.* (ATLAS Collaboration), arXiv:0901.0512 [hep-ex].

[49] U. Dersch *et al.* (SELEX Collaboration), Nucl. Phys. B **579**, 277 (2000).

[50] C. Alt *et al.* (NA49 Collaboration), Eur. Phys. J. C **49**, 897 (2007).

[51] M. Baker and K. A. Ter-Martirosian, Phys. Rep. **28**, 1 (1976).

[52] S. Ostapchenko, arXiV:hep-ph/0501093.

[53] M. Braun, Sov. J. Nucl. Phys. **52**, 164 (1990); V. A. Abramovsky and G. G. Leptoukh, *ibid.* **55**, 903 (1992); M. Hladik *et al.*, Phys. Rev. Lett. **86**, 3506 (2001).